OE Optical Engineering

TUTORIAL

Optical communications in turbulence: a tutorial

Larry B. Stotts[a,*] and Larry C. Andrews[b]
[a]Science and Technology Associates, Arlington, Virginia
[b]University of Central Florida, College of Optics, Center for Research in Electro-Optics and Lasers, Townes Laser Institute, Orlando, Florida, United States

ABSTRACT. We provide a tutorial on how to create link budgets and bit error rate (BER) and probability of fade calculations for optical communications systems designed to operate in the turbulent channel. It reviews the characterization models necessary for either incoherent or coherent free space optical communications uplink, downlink, and horizontal system analyses in the turbulent channel. Beam wander, scintillation, and receiver noise variance as well as pointing and tracking effects were included in this paper. Comparisons among these models, computer simulations and field measurements are provided throughout the paper. Good agreement is shown among all. An example analysis was provided using this information. The conclusion is that no matter whether the system is incoherent or coherent and/or which signaling format is used, the scintillation index will peg the BER to constant value at high signal-to-noise ratio well above the desired value. Other turbulence mitigation techniques must be employed to get the desired system performance.

 [DOI: 10.1117/1.OE.63.4.041207]

Keywords: free space optical communications; erbium doped fiber amplifier; turbulence; fiber coupling

Paper 20230405SSV received Apr. 28, 2023; revised Nov. 16, 2023; accepted Nov. 17, 2023; published Dec. 8, 2023.

1 Introduction

Optical communications (OC) have attracted new interests in the recent decades as high data rate airborne- and satellite-based backhaul capabilities for large capacity communication networks.[1–8] Although radio frequency (RF) systems have dominated the communications backhaul market, decreasing RF spectrum availability and network security make OC systems more attractive. Specifically, OC systems have reemerged after three decades of dormancy because of new technologies recently available from the fiber optic communications (FOC) community, such as fiber lasers and high-speed detectors. The result is that these systems provide some inherent advantages over RF communications, e.g., compact terminal size, low power consumption, substantial increase in bandwidth, unlicensed optical spectrum, and no electromagnetic interference.[1,2] However, optical signals are subject to various undesirable phenomena, including turbulence-induced signal fading, beam wander effects, and noise caused by light due to sunlight and sky radiance.[3] Fortunately, turbulence mitigation under high turbulence conditions has been successfully achieved using new system and network technologies.[7,8] The question is why some folks are successful in mitigating turbulence effects while others are not.

In most of the early communications link analyses, researchers only paid attention to signal degradation and produced ways of potentially reducing or eliminating phase perturbations to reduce scintillation and increase signal power. Techniques such as aperture averaging and emerging technologies such as adaptive optics were employed with some success.[9–11] Aperture

*Address all correspondence to Larry B. Stotts, lbstotts@gmail.com

averaging worked well for large receiver apertures and downlink/horizontal geometries. Uplinks experienced large beam wander that aperture averaging could not help reducing. Adaptive optics worked well for weak turbulent conditions or short ranges but proved ineffective in moderate to strong turbulent conditions.[12] This is because these turbulent conditions are dominated by turbulent phase fluctuations while moderate to strong conditions or longer ranges are dominated by amplitude scintillation that needs more than just phase correction.[9–12] What was missing from these analyses was the turbulent-intensity noise variance that also affected communications performance. This omission was the reason many of the analyses did not match experimental field results. Andrews and Phillips recognized this void in Ref. 9 and produced a signal-to-noise ratio (SNR) correction to account for this additional noise term. However, they did not address how this impacted the probability bit error/bit error rate (BER), or the fact that turbulence did not obey Gaussian statistics questioning whether the addition was valid as derived.

This paper is a tutorial on optical communications in turbulence that resolves these issues and shows how link budget analyses should be done. It will validate Andrews and Phillips's SNR correction and that its inclusion in the SNR equation dramatically affects communications system performance. Specifically, this paper will begin with a discussion of the origin of the SNR, then move to the validity of the Andrews and Phillips's SNR correction and establishment of the scintillation index as the key turbulent-intensity noise variance. In addition, this paper will develop the scintillation indices for uplink, downlink, and horizontal communications link geometries, which also include tracking and untracked receiver effects. An example analysis was provided using this information. The key aspect of this tutorial is that no matter whether the system is incoherent or coherent and/or which signaling format is used, the scintillation index will peg the BER to constant value at high SNR well above the desired value. Other turbulence mitigation techniques must be employed to get the desired system performance.

2 Electrical Signal-to-Noise Ratio and BER in Incoherent Optical Communications

Statistical detection and estimation theory revolutionized the fields of RF communications and remote sensing, beginning with S. O. Rice's seminal paper entitled "The Mathematical Analysis of Random Noise."[13] However, the benefit of this theory to electro-optical systems was not recognized until the 1960s. Mandel[14] and Helstrom[15] published arguably the first key papers in the area and Papoulis[16] came out with the first key textbook in the area. The effects of turbulence on communications and remote sensing emerged in the literature around the same time, e.g., Ref. 17. Andrews and Phillips were one of the first to summarize the research characterizing the effects of turbulence on laser radar and communications system performance,[9,10] and Andrews and Beason recently updated our understanding of system performance effects in these areas.[11]

This section discusses the origin of the SNR, the validity of the Andrews and Phillips's SNR correction, and the scintillation index as the key turbulent-intensity noise variance.

2.1 Origin of the Signal-to-Noise Ratio

Radar research during World War II showed that system noise negatively affected a receiver's output signal, hence, a target's detectability. This led to matched filter detection and SNR as the means and measure to quantify the signal level above the noises.[18] In 1953, Middleton advocated the detection of signals using statistical decision theory,[19] whereas Peterson et al.[20] advanced this approach with the likelihood ratio shortly thereafter. This section follows Ref. 21, pp. 102–106.

The SNR is derived from determining the signal measurement x that will be used to decide between two hypotheses, H_0 (null hypothesis) and H_1 (signal-present hypothesis). Considering that any measurement can create errors, we need to treat the outcome of any decision strategy as a random variable that is governed by the probability densities functions (PDF) $p_0(x)$ and $p_1(x)$ for hypotheses H_0 and H_1, respectively. In general, the PDFs for hypotheses H_0 and H_1 can be written as

$$p_j(x) = \frac{1}{\sqrt{2\pi n_0}} e^{-(x-\mu_j)^2/2n_0} \quad j = 0,1, \tag{1}$$

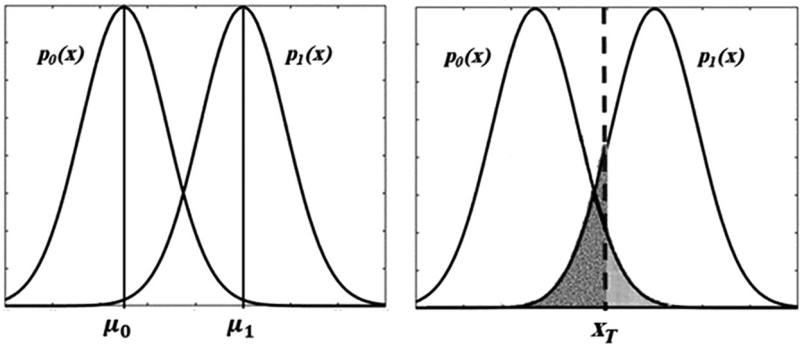

Fig. 1 (a) PDFs for hypotheses H_0 and H_1, pinpointing mean levels, μ_0 and μ_1, respectively, and (b) same PDFs with threshold x_T.

respectively. In the above equation, the parameters $\{\mu_j; j = 0,1\}$ are the means assuming $\mu_0 < x < \mu_1$, and n_0 is the unilateral spectral noise density for Gaussian PDFs of the two possible hypotheses. Figure 1(a) shows a comparison of the two PDFs.

Hypothesis H_0's PDF implies that the measured value for x comes from the noise distribution and has an averaged value of μ_0 and variance n_0. Equation (1) implies that x will vary around the averaged value most of the time (values near the peak), but also will occasionally be extremely different (values at the tails). One will see similar measurement deviations occurring with hypothesis H_1's PDF, but around an average value of μ_1, rather than μ_0. The question one might ask is how often each PDF occurs? The fraction of time that H_0 happens is ζ_p and is called the prior probability for this hypothesis. Alternately, the fraction of time that H_1 happens is consequently $(1 - \zeta_p)$ and is called the prior probability for that hypothesis.

Given all the above, what is the strategy for deciding between hypotheses H_0 and H_1, assuming a measurement x? The obvious choice is that a decision maker picks a value of x, say x_T, and then chooses hypothesis H_0 when $x \leq x_T$ and hypothesis H_1 for $x > x_T$ [see Fig. 1(b)]. That makes senses until you wonder, "How did you pick x_T?" Obviously, the presence of noise causes mistakes to be made in the decision process. This suggests that the decision threshold is the value of x_T to minimize any negative effects caused by making mistakes. How do we determine the desired value for x_T?

The Neyman–Pearson decision strategy is designed for deciding when hypothesis H_1 occurs rarely and H_0 dominates the decision process, which is normally true for sonar, radar, optical, and electro-optical systems doing real world surveillance. This strategy essentially comes down to maximizing the probability of detection of a target while minimizing the false-alarm probability. The probability of detection (P_d) is given as

$$P_d = 1 - Q_1 = 1 - \int_{-\infty}^{x_T} p_1(x)\mathrm{d}x = \int_{x_T}^{\infty} p_1(x)\mathrm{d}x, \tag{2}$$

and the probability of false alarm (FA) equals

$$P_{\mathrm{FA}} = Q_0 = \int_{x_T}^{\infty} p_0(x)\mathrm{d}x. \tag{3}$$

The parameters Q_0 and Q_1 represent "the error of the first kind" and the "error of the second kind," respectively. Referring again to Fig. 1(b), Q_0 is the shaded area under the $p_0(x)$ curve to the right of x_T and Q_1 is the shaded area under the $p_1(x)$ curve to the left of x_T.

To implement this strategy based on a single measurement x, we calculate the likelihood ratio $\Lambda(x) = p_1(x)/p_0(x)$ and compare the result to some threshold value Λ_T. If $\Lambda(x) \leq \Lambda_T$, the decision maker picks hypothesis H_0; if $\Lambda(x) > \Lambda_T$, the decision maker selects hypothesis H_1. The computed likelihood ratio is a random variable and has a probability density function (PDF) $P_0(\Lambda)$ under hypothesis H_0. It is related to the known PDF as follows:

$$P_0(\Lambda)d\Lambda = p_0(x)dx. \tag{4}$$

The probability P_{FA} therefore can be written as

$$P_{\mathrm{FA}} = \int_{\Lambda_T}^{\infty} P_0(\Lambda)\mathrm{d}\Lambda. \tag{5}$$

The value of Λ_T is established by pre-assigning a value to Q_0 and inverse computing it. The probability of detection P_d is then determined by calculating

$$P_d = \int_{\Lambda_T}^{\infty} P_1(\Lambda)\mathrm{d}\Lambda, \tag{6}$$

where $P_1(\Lambda)$ is the PDF under hypothesis $H1$. The results of these computations generally are portrayed in single figure, plotting the detection probability (power of the test) as a function of the FA probability (size of the test). This curve is often called the "receiver operating characteristic" or "ROC" curve. The choice between the two possible hypotheses can be based not only on the likelihood ratio $\Lambda(x)$ but also on monotonic function $\Upsilon = \Upsilon(\Lambda(x))$ of the likelihood ratio, called the "test statistic." This implies that

$$P_{\mathrm{FA}} = \int_{\Upsilon_T}^{\infty} P_0(\Upsilon)\mathrm{d}\Upsilon, \tag{7}$$

and

$$P_d = \int_{\Upsilon_T}^{\infty} P_1(\Upsilon)\mathrm{d}\Upsilon. \tag{8}$$

As noted in the last section, the best SNR comes from matched-filtering the incoming signal to the initial transmitted waveform. If we assume a known (deterministic) signal, say $s(t)$, to be detected in additive white Gaussian noise, then our desired test statistic can be written as

$$\Upsilon = \int_0^T s(t)x(t)\mathrm{d}t, \tag{9}$$

where Υ is the decision test statistic, T is the receiver integration time, and $v(t)$ is the input voltage. Using this statistic, we find that

$$E\{\Upsilon|H_1\} = \int_0^T s(t)x(t)\mathrm{d}t|_{v(t)=s(t)} = \int_0^T |s(t)|^2\mathrm{d}t = E_s, \tag{10}$$

and

$$E\{\Upsilon|H_0\} = \int_0^T s(t)x(t)\mathrm{d}t|_{v(t)=n(t)} = 0, \tag{11}$$

where E_s is the energy of the received signal and $n(t)$ is the receiver noise in the absence of an incoming signal with a variance proportional to $N_0/2$. (The average noise level $\langle n(t)\rangle = 0$.) The variance of Υ is given as

$$\mathrm{Var}\,\Upsilon = n_0 = \int_0^T \int_0^T s(t_1)s(t2)\langle n(t_1)n(t_2)\rangle \mathrm{d}t_1\mathrm{d}t_2 \tag{12}$$

$$= \frac{N_0}{2}\int_0^T \int_0^T s(t_1)s(t2)\delta(t_2 - t_1)\mathrm{d}t_1 dt_2 \tag{13}$$

$$= \frac{N_0}{2}\int_0^T |s(t)|^2\mathrm{d}t = N_0E_s/2. \tag{14}$$

Using the above equations, we can write the PDFs for hypotheses H_1 and H_0 as

$$p_1(\Upsilon) = \frac{1}{\sqrt{\pi N_0 E_s}} e^{-(\Upsilon - E_s)^2/N_0E}, \tag{15}$$

and

$$p_0(\Upsilon) = \frac{1}{\sqrt{\pi N_0 E_s}} e^{-\Upsilon^2/N_0 E}, \tag{16}$$

respectively.

The FA and detection probabilities then are given as

$$P_{\mathrm{FA}} = Q(x_T), \tag{17}$$

and

$$P_d = Q\left(x_T - \sqrt{\mathrm{SNR}}\right), \tag{18}$$

respectively, where

$$Q(y) = \frac{1}{\sqrt{2\pi}} \int_y^\infty e^{-q^2/2} \mathrm{d}q \tag{19}$$

is the Q-function [$= 0.5 erfc(x/\sqrt{2})$, with $erfc(x)$ being the complementary error function],

$$x_T = \Upsilon_0 \sqrt{2/N_0 E_s}, \tag{20}$$

is the decision threshold, and

$$\mathrm{SNR} = \frac{[E\{\Upsilon | H_1\}]^2}{\mathrm{Var}\,\Upsilon} = \frac{2E_s}{N_0}. \tag{21}$$

There is an important linkage to be made between energy and information transfer using Eq. (21). In his seminal paper on communications, Shannon[22] assumed a signal space defined by a dimension $2B_eT$ (defined as the number of Nyquist samples of a function band-limited to electrical bandwidth $B_e = 1/2T$, and observed over the time T). This means one can rewrite Eq. (21) as

$$\mathrm{SNR} = \frac{2E_s}{N_0} = \left(\frac{R_b T}{R_b T}\right) \frac{2E_s}{N_0} = (R_b 2T) \frac{E_b}{N_0} = \frac{R_b}{B_e} \frac{E_b}{N_0} = r \frac{E_b}{N_0}, \tag{22}$$

where R_b is the communications data rate in bits per second (bps), $E_b = E_s/R_bT$ is the energy per bit in joules per bit, $r = R_b/B_e = \log_2(M_{\mathrm{symbol}})$ is the system's spectral efficiency in bits per second per Hertz (bps/Hz), and M_{symbol} is the number of symbols in the communications alphabet.

2.2 Signal-to-Noise Ratio in a Direct Detection System

In most communications system analyses, Eq. (21) is written as

$$\mathrm{SNR}_e = \frac{2E_s}{N_0} \left(\frac{2T}{2T}\right) = \frac{E_s/T}{N_0 B_e} = \frac{P_s}{P_n} = \frac{i_s^2}{i_n^2} = \frac{R_\lambda^2 \overline{P}_{\mathrm{rec}}^2}{i_n^2}, \tag{23}$$

where P_s is the average electrical signal power, P_n is the average electrical noise power, i_s is the average signal current, i_n is the total average noise current, R_λ is the responsivity of the receiver's photodetector in amperes per watt (A/W), and $\overline{P}_{\mathrm{rec}}$ is the incoming signal mean power impinging an optical detector, which includes all the diffraction, refraction, and any atmospheric loss. The incoming received power is given as

$$P_{rx} \approx \gamma_{tx} \gamma_{rx} P_{tx} \left[\frac{A_{tx} A_{rx}}{(\lambda R)^2}\right] = \gamma_{tx} \gamma_{rx} P_{tx} \mathrm{FSL}, \tag{24}$$

where γ_{tx} is the transmitter transmittances, γ_{rx} is the receiver transmittances, $\mathrm{FSL} = A_{tx}A_{rx}/(\lambda R)^2$ is the Fraunhofer spreading loss (FSL), P_{tx} is the transmitter laser power, $A_{tx} = \pi D_{tx}^2/4$, D_{tx} is the transmitter aperture diameter, $A_{rx} = \pi D_{rx}^2/4$, D_{rx} is the receiver aperture diameter, λ is the laser wavelength, and R is the link range. Let us now talk about the detected average noise power. Equation (24) is called the Friis optical range equation.

In RF communications, one only deals with thermal noise within the RF receiver. Its spectral density is given by $N_0 = k_B T_0$, where $k_B = 1.38 \times 10^{-23}$ J/K is Boltzmann's constant, and T_0 is

the receiver temperature in degrees Kelvin [K]. It obeys Gaussian statistics. One also has thermal noise to contend with in optical receivers, which obeys Gaussian statistics like in the RF case. Specifically, the thermal noise current PDF is given as

$$P_{\text{th}}(P) = e^{-(P-\overline{P}_{\text{th}})^2/2\sigma_{\text{th}}^2}, \tag{25}$$

where P is the received power by the detector, $\overline{P}_{\text{th}}$ is the average thermal power, and $\sigma_{\text{th}}^2 = 4k_bT_0B_e$ is the thermal noise power variance. In an optical receiver, one generally creates a photo-electron current $i(t)$ that translates into electrical power via the equation $P(t) = i^2(t)R_L$, where R_L is the receiver's load resistor in ohms.

On the other hand, dark current in an optical receiver is a Poisson process. It can be shown that the dark current Poisson PDF is written as

$$P_{\text{DC}}(K) = \frac{\mu_{\text{DC}}^K e^{-\mu_{\text{DC}}}}{K!}, \tag{26}$$

where $\mu_{\text{DC}} = 2qi_{\text{DC}}R_LB_e$, $q = 1.602 \times 10^{-19}$ coulombs (C) is the charge on an electron, and i_{DC} is the receiver's mean dark current.

For large K, Eq. (26) tends toward a Gaussian PDF given as

$$P_{\text{DC}}(K \to P) \approx \frac{1}{\sqrt{2\pi\mu_{\text{DC}}}} e^{-(P-\overline{P}_{\text{DC}})^2/2\mu_{\text{DC}}}. \tag{27}$$

Mathematically, this can be shown using Stirling's equation (Ref. 3, pp. 329–330). Figure 2 shows Eq. (26) as a function of K for values of $\mu_{\text{DC}} = \overline{P}_{\text{th}} = 30$,50, and 100. From this figure, one can see that $\mu_{\text{DC}} \geq 30$ electrons, which is typical for most systems, creates Poisson and Gaussian PDFs that match well.

Now, both thermal and dark current exist in an optical receiver whether an incoming signal is present or not. They are created by separate, independent physical mechanisms, so they are independent random variables in the photo-electron creation process (chapter 8 in Ref. 3). This means that the combined effect of both is derived from the "sum of random variables" theory.[23] The combined PDF comes from the convolution of Eqs. (24) and (26). The result is another Gaussian PDF with a mean of $\overline{P}_{\text{thermal}} + \overline{P}_{\text{DC}}$ and a variance of $4k_bT_0B_e + 2qi_{\text{DC}}R_LB_e$.

Now, both thermal and dark current exist in an optical receiver whether an incoming signal is present or not. They are created by separate, independent physical mechanisms, so they are independent random variables in the photo-electron creation process (chapter 8 in Ref. 3). This means that the combined effect of both is derived from the "sum of random variables" theory.[23] The combined PDF comes from the convolution of Eqs. (25) and (27). The result is another Gaussian PDF with a mean of $\overline{P}_{\text{thermal}} + \overline{P}_{\text{DC}}$ and a variance of $4k_bT_0B_e + 2qi_{\text{DC}}R_LB_e$.

Now, what happens when external light enters an optical receiver? One gets "signal-shot-noise" in addition to the dark current and thermal noise in the receiver. All photodetectors create this photon fluctuation noise, even when the light input is constant in intensity. This is quantum

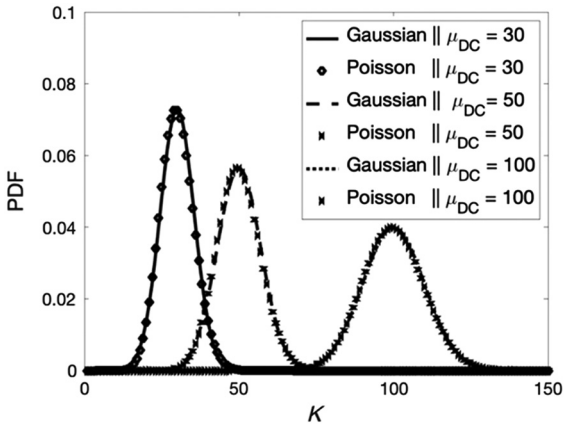

Fig. 2 Comparison of Poisson and Gaussian PDFs as a function of K for various values of μ_{DC}.

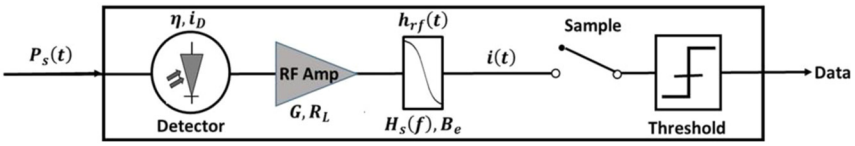

Fig. 3 Schematic of a DD optical receiver.

mechanical effect and comes from the random emission of photoelectrons derived from the external light absorption by the detector. Like dark current, it is a Poisson process and tends toward Gaussian statistics as the mean current increases and becomes appropriate as an approximation around 30 photo-electrons. The two primary external light sources are the transmitted signal beam and scattered solar radiation. Again, using the "sum of random variables" theory, the resulting Gaussian PDF has variance

$$\sigma^2_{\text{total}} = 2qR_\lambda \overline{P}_{\text{rec}} R_L B_e + 2qR_\lambda \overline{P}_{\text{bkg}} R_L B_e + 2qi_{\text{DC}} R_L B_e + 4k_b T_0 B_e, \tag{28}$$

and mean

$$\mu_{\text{total}} = \overline{P}_{\text{th}} + \overline{P}_{\text{DC}} + \overline{P}_{\text{rec}} + \overline{P}_{\text{bkg}}, \tag{29}$$

where $\overline{P}_{\text{rec}}$ is the received optical solar background mean noise power before the detector. Let us look at direct detection (DD) communications receiver.

Figure 3 illustrates a basic DD receiver layout with a p-type—intrinsic—n-type (PIN) photodiode. It has an incoming signal $P_s(t)$ impinges an optical detector and is changed into current that get electrically amplified in an RF amplifier. At this stage, one denotes its gain by G, its quantum efficiency η, and its load resistor as R_L. This current is then subjected to post-detection filtering with impulse response $h_{\text{rf}}(t)$ and effective electrical bandwidth B_e. This filtered result then passes through sample-and-hold circuitry before yielding the result, communications data.

The electrical SNR for this type of system is given as

$$\text{SNR}_e = \frac{G^2 R_\lambda^2 R_L P_{\text{rec}}^2}{2qB_e G^2 [R_\lambda (P_{\text{rec}} + P_b) + i_D] R_L + 4k_B T_0 F_{\text{rf}} B_e} \tag{30a}$$

$$= \frac{P_{\text{rec}}^2}{2qB_e [(P_{\text{rec}} + P_b)/R_\lambda + i_D/R_\lambda^2] + 4k_B T_0 F_{\text{rf}} B_e / G^2 R_\lambda^2 R_L}, \tag{30b}$$

where F_{rf} is its amplifier's noise factor. Looking at Eq. (18), we see that that the probability of detection is a function of the square root of the electrical SNR, which is true in general. The optical community likes to use the optical signal to noise ratio (OSNR) in their link budget analyses, which is defined as

$$\text{OSNR} = \sqrt{\text{SNR}_e} = \frac{P_{\text{rec}}}{\sqrt{2qB_e [(P_{\text{rec}} + P_b)/R_\lambda + i_D/R_\lambda^2] + 4k_B T_0 F_{\text{rf}} B_e / G^2 R_\lambda^2 R_L}}. \tag{31}$$

We will use this convention for the rest of the paper. This means that Eq. (18) can be rewritten as

$$P_d = Q(x_T - \text{OSNR}). \tag{32}$$

On the other hand, if one has an avalanche photodiode (APD) detector instead of the PIN photodiode, the optical SNR is written as

$$\text{OSNR} = \frac{P_{\text{rec}}}{\sqrt{2qF_{\text{APD}} B_e [(P_{\text{rec}} + P_b)/R_\lambda + i_D/R_\lambda^2] + 4k_B T_0 F_{\text{rf}} B_e / G^2 R_\lambda^2 R_L}}, \tag{33}$$

where F_{APD} is the excess noise factor associated with the variation in gain G. The excess noise factor equals

$$F_{\text{APD}}(G, k_{\text{ion}}) = G\left[1 - (1 - k_{\text{ion}})\left(\frac{G-1}{G}\right)^2\right], \tag{34}$$

Table 1 Excess noise factor for various detector material types.

Detector type	Ionization ratio	Typical gain	Excess noise factor
Silicon "reach-through"	0.02	150	4.9
Silicon "SLiK low k"	0.002	500	3.0
Germanium	0.9	10	9.2
InGaAs	0.45	10	5.5

where k_{ion} is the APD's effective ionization coefficient ratio. Table 1 depicts excess noise factors for various detector material types.

2.3 *Q*-Parameter

Figure 1 showed a typical data input scenario for the detection threshold decision process. An incoming signal is determined via some mechanism during a synchronized time interval T_1 to establish whether either a "1" or a "0" is transmitted. The BER is the number of bit errors per unit time. That is, the number of bit errors divided by the total number of transferred bits during a studied time interval. It is a unit-less performance measure, often expressed as a percentage. On the other hand, the bit error probability P_{BE} is the expected value for the BER. The BER can be considered as an approximate estimate of the bit error probability. This estimate is accurate for a long-time interval and a high number of bit errors measured. We will not distinguish between the two in the discussions to come as most people consider them synonymous.

If the optical receiver is a maximum *a posteriori* (MAP) receiver, then the BER is given as

$$\text{BER} = \zeta_p \Pr\{1|0\} + (1-\zeta_p)\Pr\{0|1\}, \tag{35}$$

where ζ_p and $(1-\zeta_p)$ are the *a priori* probabilities of receiving a "1" or a "0," respectively, and $\Pr\{1|0\}$ and $\Pr\{0|1\}$ are conditional probabilities representing the respective probability of falsely declaring the first argument true, when the second argument actually is true. If we assume equal *a priori* probabilities, then Eq. (35) reduces to

$$\text{BER} = 0.5\ \Pr\{1|0\} + 0.5\ \Pr\{0|1\}. \tag{36}$$

Let us assume the photo-current for the bits "1" and "0" equals i_1 and i_0, respectively. The total variance associated with each of these currents then is written as

$$\sigma_1^2 = \sigma_{1-ss}^2 + \sigma_{1\text{-thermal}}^2, \tag{37}$$

and

$$\sigma_0^2 = \sigma_{0-ss}^2 + \sigma_{0\text{-thermal}}^2, \tag{38}$$

respectively. Since the average photo-current is different for the bits "1" and "0," the associated average shot noise current and its variance will be different, i.e., $i_1 > i_0$, which implies that $\sigma_1^2 \neq \sigma_0^2$. Let i_{th} represent the decision threshold. The conditional probabilities can be written as

$$\Pr\{1|0\} = \frac{1}{\sqrt{2\pi\sigma_0^2}} \int_{i_{\text{th}}}^{\infty} e^{-(i-i_0)^2/2\sigma_0^2} \mathrm{d}i = 0.5 erfc\left((i_{\text{th}} - i_0)/\sqrt{2\sigma_0^2}\right), \tag{39}$$

and

$$\Pr\{0|1\} = \frac{1}{\sqrt{2\pi\sigma_1^2}} \int_{-\infty}^{i_{\text{th}}} e^{-(i-i_1)^2/2\sigma_1^2} \mathrm{d}i = 0.5 erfc\left((i_1 - i_{\text{th}})/\sqrt{2\sigma_1^2}\right), \tag{40}$$

under the Gaussian statistics assumption. Substituting Eqs. (39) and (40) into Eq. (36) yields

$$\text{BER} = 0.25\, erfc\left((i_{\text{th}} - i_0)/\sqrt{2\sigma_0^2}\right) + 0.25\, erfc\left((i_1 - i_{\text{th}})/\sqrt{2\sigma_1^2}\right). \tag{41}$$

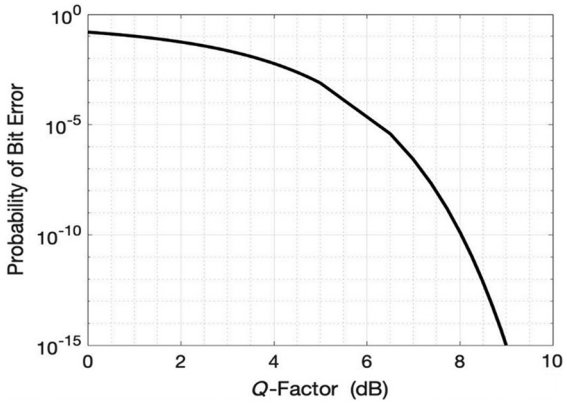

Fig. 4 BER versus Q-parameter.

The current threshold that minimizes the BER given in Eq. (41) is

$$i_{\text{th}} \approx \frac{\sigma_0 i_1 + \sigma_1 i_0}{(\sigma_1 + \sigma_0)}, \tag{42}$$

assuming the system's thermal or pre-amplifier noise is the largest components in both σ_1^2 and σ_0^2.

Substituting Eq. (42) into either of the two arguments contained in Eq. (41), we create what is called the Q-parameter, which is given as

$$Q \approx \frac{(i_1 - i_0)}{(\sigma_1 + \sigma_0)}. \tag{43}$$

The Q-parameter is a measure of the OSNR. Using Eq. (43), Eq. (41) reduces to

$$\text{BER} \approx 0.5\, erfc\left(Q/\sqrt{2}\right) \approx \frac{1}{Q\sqrt{2\pi}} e^{-Q^2/2}, \tag{44}$$

where the approximation in Eq. (44) is valid for $Q > 3$. Figure 4 shows this BER as a function of the Q-parameter. For a BER $= 10^{-12}$, $Q = 7$ or 8.45 dB.

2.4 Receiver Sensitivity

Let us assume direct-detection communications using a PIN photodiode. Without loss of generality, we will let $i_0 = 0$, which translates into the zero-signal power transmitted for a bit "0," $G = 1$ (normally true for PIN-detectors), $P_b = 0$, and no atmospheric loss.

In a 10 Gigabit per second (Gbps) intensity-modulated/DD PIN receiver, the key noise sources typically are thermal, dark current-induced, and signal-shot noises. Using Eq. (43), the associated Q parameter is given as

$$Q_{\text{IM}} = \frac{2R_\lambda P_{\text{rec}}}{\sqrt{2qB_e[2R_\lambda P_{\text{rec}} + i_D] + 4kT_0 F_{\text{rf}} B_e / R_L} + \sqrt{2qB_e i_D + 4kT_0 F_{\text{rf}} B_e / R_L}}. \tag{45}$$

Figure 5 plots this Q-parameter in decibels as a function of received average optical signal power for a 10 Gbps PIN system with $\lambda = 1.55$ μm, $R_\lambda = 0.85$ A/W, $R_L = 50$ Ω, $i_D = 5$ nA, $F_{\text{rf}} = 1$, $T_0 = 300$ K, and $B_e = 7.5$ GHz. If the system requirement is a BER $= 10^{-12}$, this figure shows that the associated Q-factor of 8.45 dB implies a minimum average power $P_{\text{avg}}^{\text{min}}$ to achieve that BER is −19 dBm (decibel-milliwatt) for the system parameters given. This minimum average power $P_{\text{avg}}^{\text{min}}$ is called the receiver sensitivity. From this plot, we also see that a dB reduction in minimum average signal power decreases the Q-parameter by a dB. Let us look at an emerging system approach that has some benefits to turbulence mitigation that we see later in the paper.

To improve communications link performance, some optical engineers add an optical predetection optical amplifier, such as an erbium-doped fiber amplifier (EDFA), in front of the PIN photodiode. An EDFA increases the incoming received signal but also will create optical input noise at the detector. The induced noise comes from both spontaneous and stimulated emissions

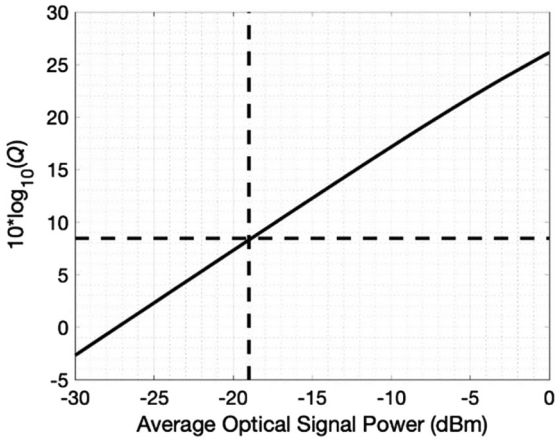

Fig. 5 Receiver sensitivity versus average optical signal power for a 10 Gbps PIN system.

in the fiber amplifier but can be reduced by optical filtering before the detector. Unfortunately, it cannot be reduced totally.[24] We now find the three optical noise powers (variances) are

(1) Signal-shot noise

$$\sigma_{\text{shot}}^2 = 2qB_e G i_{\text{avg}} R_L \approx 2qB_e G[2\eta P_{\text{avg}}/h\nu]. \tag{46}$$

(2) The signal-spontaneous beat noise variance, which is given as

$$\sigma_{\text{sig-sp}}^2 = 2Gi_{\text{avg}} i_{\text{sp}} R_L B_e / B_0, \tag{47}$$

$$= 2h\nu NF_{\text{opt}} G(G-1)(2R_\lambda^2 P_{\text{avg}}) R_L B_e, \tag{48}$$

with $NF_{\text{opt}} = 2n_{\text{sp}}$ being the EDFA optical noise figure and n_{sp} being the EDFA inversion parameter, and (3) the spontaneous-spontaneous beat noise variance, which is equal to

$$\sigma_{\text{sp-sp}}^2 = i_{\text{sp}}^2 R_L [B_e(2B_o - B_e)]/(2B_0^2) \tag{49}$$

$$= 0.5[R_\lambda h\nu NF_{\text{opt}}(G-1)]^2 R_L B_e(2B_0 - B_e), \tag{50}$$

where B_0 is the optical bandwidth of the receiver.[24] Here, $i_{\text{avg}} = q\eta P_{\text{avg}}/h\nu = R_\lambda P_{\text{avg}}$, and i_{sp} is the photocurrent generated by the spontaneous emissions (including both polarizations) at the output of the detector, which equals

$$i_{\text{sp}} = 2q\eta n_{\text{sp}} B_0(G-1) = q\eta NF_{\text{opt}} B_0(G-1) = R_\lambda h\nu NF_{\text{opt}} B_0(G-1). \tag{51}$$

The resulting Q-parameter is then

$$Q_{\text{ERDA}} = \frac{2R_\lambda G P_{\text{rec}}}{\sqrt{2qB_e[2R_\lambda G P_{\text{rec}} + i_D] + \sigma_{\text{sig-sp}}^2 + \sigma_{\text{sp-sp}}^2 + 4kT_0 F_{\text{rf}} B_e/R_L} + \sqrt{2qB_e i_D + \sigma_{\text{sp-sp}}^2 + 4kT_0 F_{\text{rf}} B_e/R_L}}. \tag{52}$$

The product GP_{avg} is the amplified average optical signal power necessary for "1" bit. Figure 6 plots receiver sensitivity as a function of average optical signal power for a 10 Gbps EDFA-PIN system for noise variance conditions. Here, we have $GP_{\text{avg}} = 0$ dBm, $Q_{\text{ERDA}} = 7$, $\lambda = 1.55$ μm, $R_\lambda = 0.85$ A/W, $R_L = 50$ Ω, $i_D = 5$ nA, $F_{\text{rf}} = 1$, $T_0 = 300$ K, $B_e = 7.5$ GHz, $B_0 = 25$ GHz, and $n_{\text{sp}} = 1.58$ [$NF_{\text{opt}} \simeq 5$ dB]. (The dark-current Q-factor is ~54 dB and is not shown on the chart.)

It is clear from this figure that the receiver sensitivity $P_s^{\min} \approx -40$ dBm for the system parameters given. This is >20 dB better than PIN diode system shown above. It also shows that thermal and signal-shot noises are within a couple of dBs of each other, but much weaker than either

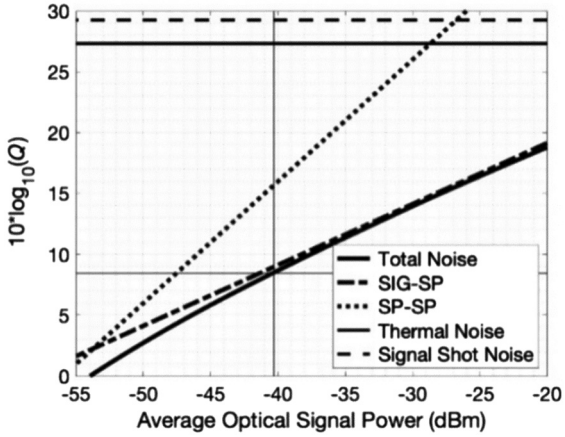

Fig. 6 Receiver sensitivity versus average optical signal power for a 10 Gbps EDFA system.

stimulated-spontaneous and spontaneous-spontaneous beat noises. In addition, we see that a dB reduction in average signal power decreases the Q-factor by around 2/3 of a dB. Finally, the figure indicates that the stimulated-spontaneous beat noise becomes much stronger than the other noises sources when the average signal power exceeds -45 dBm.

Looking at the results in Fig. 6, the ERDA-PIN system Q-parameter can be written as

$$\begin{aligned} Q_{\text{EDFA}} &\approx \frac{2R_\lambda G P_{\text{rec}}}{2\sqrt{\sigma^2_{\text{sig-sp}}}} = \frac{R_\lambda G P_{\text{rec}}}{\sqrt{2h\nu N F_{\text{opt}} G(G-1)(2R_\lambda^2 P_{\text{avg}}) B_e}} \\ &\approx \frac{P_{\text{rec}}}{\sqrt{2h\nu N F_{\text{opt}} P_{\text{avg}} B_e}} = \sqrt{\frac{\eta P_{\text{rec}}}{2h\nu B_e}\left[\frac{1}{\eta N F_{\text{opt}}}\right]} = \sqrt{\frac{\text{SNR}_{\text{QL}}}{\eta N F_{\text{opt}}}}, \end{aligned} \tag{53}$$

for $G \geq 15$. It is easy to show that

$$\text{SNR}_{\text{EDFA}} = \frac{\text{SNR}_{\text{QL}}}{\eta n_{\text{sp}}} = Q^2_{\text{EDFA}}, \tag{54}$$

and the receiver sensitivity is

$$P^{\text{min}}_{\text{avg}} = \frac{Q_{\text{EDFA}}\sqrt{\sigma^2_{\text{sig-sp}}}}{R_\lambda G}. \tag{55}$$

The asymptotic behavior of the electrical SNR is shown in Fig. 7, which is an illustration of the various noise powers and the electrical SNRs from classical calculations. Here, we have $P_{\text{avg}} = -30$ dBm, $Q_{\text{ERDA}} = 7$, $\lambda = 1.55$ μm, $R_\lambda = 0.85$ A/W, $R_L = 50$ Ω, $i_D = 5$ nA,

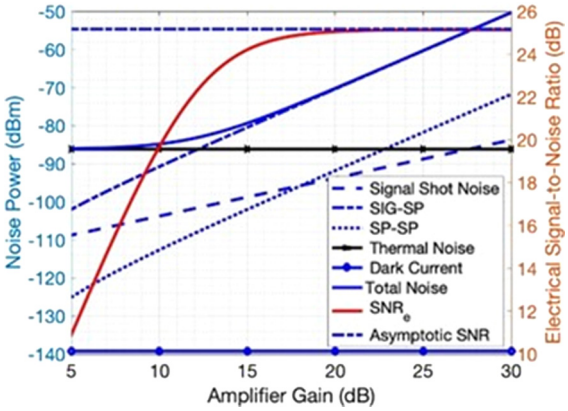

Fig. 7 Various noise powers and SNRs as a function of EDFA amplifier gain.

$F_{\text{rf}} = 1$, $T_0 = 290$ K, $B_e = 7.5$ GHz, $B_0 = 75$ GHz, and $n_{\text{sp}} = 1.58$ [$NF_{\text{opt}} \simeq 5$ dB]. This figure clearly shows the dominate behavior of signal-spontaneous beat noise variance for $G \geq 15$.

2.5 Electrical Signal-to-Noise Ratio in Free Space with Link Tracking Errors

This section provides the basic equations for analyzing link performance of an optical communications system experiencing pointing and tracking errors induced by the link's transmitter and receiver platforms. This section follows Refs. 25 and 26.

2.5.1 *Received power equation*

The average received optical signal power for a satellite communications cross-link in the presence of jitter can be written as

$$P_{rx} \approx \gamma_{tx}\gamma_{rx}P_{tx}\left[\frac{A_{tx}A_{rx}}{(\lambda R)^2}\right]L_{\text{jitter}}L_{pp} = \gamma_{tx}\gamma_{rx}P_{tx}FSLL_{\text{jitter}}L_{pp}, \tag{56}$$

where

$$L_{\text{jitter}} = \theta_d^2/(\theta_d^2 + \sigma^2) \equiv \text{Jitter Loss Factor}, \tag{57}$$

$$\theta_d = \lambda/D_{tx} \equiv \text{Transmitter beam spread}, \tag{58}$$

$\sigma \equiv$ rms jitter error, and $L_{pp} \equiv$ Power Penalty (because of jitter).

2.5.2 *Bit error rate in the presence of platform jitter*

Pointing errors have a significant effect on link performance and the BER. It can be shown that the PDF for the normalized received optical irradiance $p(I)$ is a beta distribution and is given as

$$p(I') = \beta I'^{\beta-1}, \quad 0 \leq I' \leq 1, \tag{59}$$

where $I' = I/\overline{I}$ is the normalized intensity, and

$$\beta = \theta_d^2/4\sigma^2. \tag{60}$$

The average intensity, $\overline{I}$, is given as

$$\overline{I} = \beta/(\beta + 1). \tag{61}$$

The unconditional BER in the presence of jitter should be averaged with respect to the above PDF to yield the average BER; specifically,

$$\overline{\text{BER}} = \int_0^1 p_j(I')\text{BER}\left(\frac{Q_r I'}{\overline{I}}\right)\text{d}I' \tag{62}$$

$$= \frac{Q_r(\beta+1)}{2}\int_0^1 I'^{\beta-1} erfc\left(\frac{Q_r I'}{\overline{I}\sqrt{2}}\right)\text{d}I', \tag{63}$$

for an NRZ OOK link with a Q-parameter specification Q_r as an example. Figure 8 shows the degradation of the $\overline{\text{BER}}$ as a function of Q_r and the ratio of beam θ_d divergence to random jitter σ.

The power penalty L_{pp} referenced previously results from the variation in received signal irradiance as it affects the average BER, which is defined as

$$L_{pp} = \left[\frac{Q|_{\text{BER}(Q)=a_{\text{BER}}}}{Q_r|_{\overline{\text{BER}}(Q_r)=a_{\text{BER}}}}\right], \tag{64}$$

where a_{BER} represents the system BER specification. Figure 9 shows the power penalty L_{pp} as a function of θ_d/σ for several specific values of a_{BER}.

As a final note, one would like to minimize the power penalty in any system design. Table 2 gives the ratio for θ_d/σ to minimize the power penalty for a collection of BERs.

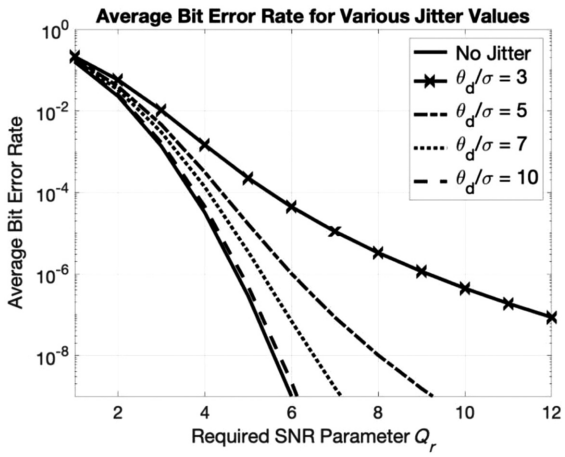

Fig. 8 Average BER as a function of the required SNR parameter and the ratio of beam θ_d divergence to random jitter σ.

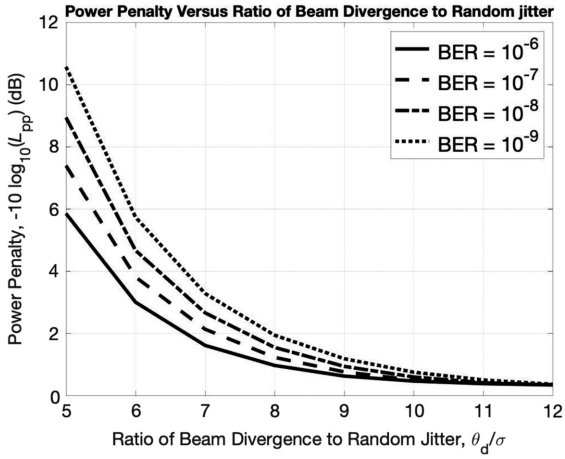

Fig. 9 The power penalty L_{pp} as a function of the ratio of beam θ_d divergence to random jitter σ.

Table 2 The optimum ratio of beam θ_d divergence to random jitter σ for a set of desired BER.

BER	$(\theta_d/\sigma)_{\text{opt}}$
10^{-2}	4.12431
10^{-3}	4.85198
10^{-4}	5.47376
10^{-5}	6.02693
10^{-6}	6.53065
10^{-7}	6.9964
10^{-8}	7.43177
10^{-9}	7.84207
10^{-10}	8.231236
10^{-11}	8.60228
10^{-12}	8.95751

2.5.3 *Optical tracking channel*

The fade statistic is needed for the optical tracking channel. Here, we use the probability of fade, which describes the percentage of time the irradiance of the received wave is below a prescribed threshold value (Ref. 10, p. 95).

As noted in Eq. (59), the PDF of the received irradiance is a beta distribution. The average received optical power for the tracking sensor is given as

$$P_{\text{rec}}^{ts} = \gamma_{ts}\gamma_{rs}P_{ts}FSL_{ts}L_{\text{jitter}}. \tag{65}$$

The fade level F_T from the average level equal

$$F_T = \left(\frac{\beta+1}{\beta}\right)P_F^{1/\beta}, \tag{66}$$

where

$$P_F = \int_0^{F_T(\beta/\beta+1)} p_j(I')\mathrm{d}I' = [F_T(\beta/\beta+1)]^\beta \tag{67}$$

is the allowable fade probability at the tracking sensor. The surge level S_T similarly is defined as

$$S_T = \left(\frac{\beta+1}{\beta}\right)[1-P_S]^{1/\beta}, \tag{68}$$

where

$$P_F = \int_{F_T(\beta/\beta+1)}^{1} p_j(I')\mathrm{d}I' = 1-[S_T(\beta/\beta+1)]^\beta \tag{69}$$

is the allowable surge probability at the tracking sensor. Figures 10 and 11 show the cumulative fade and surge probabilities are plotted as a function of fade and surge levels, respectively.

The dynamic range required for the tracking sensor to cope with only random angular jitter is given as

$$DR_{\text{jitter}} = \frac{S_T}{F_T}. \tag{70}$$

In practice, the variation of distance (due to orbital motion of the satellites) should be accounted for in the dynamic range, which changes Eq. (69) to

$$DR_{\text{total}} = \frac{S_T}{F_T}\left[\frac{R_{\max}}{R_{\min}}\right]^2, \tag{71}$$

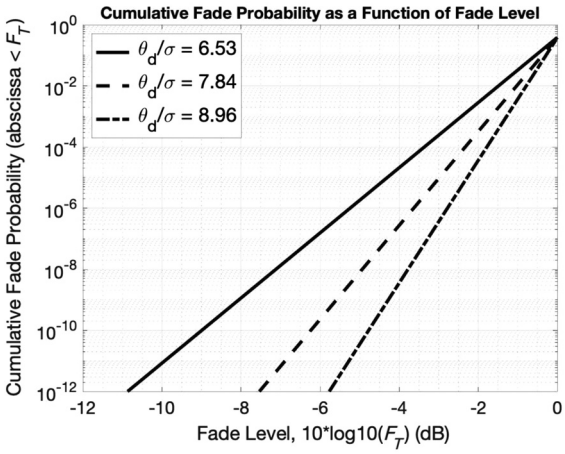

Fig. 10 Cumulative fade probability as a function of fade levels for three ratios of beam θ_d divergence to random jitter.

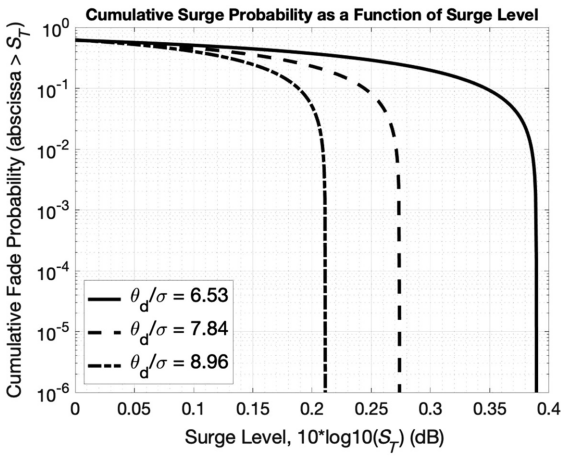

Fig. 11 Cumulative surge probability as a function of surge levels for three ratios of beam θ_d divergence to random jitter.

where $R_{\max}$ and $R_{\min}$ are the maximum and minimum ranges, respectively, between the two satellites as they traverse their orbital paths. The transmitted laser power should be adjusted as the link range changes so the dynamic range of the tracking sensor is less than DR_{total}.

2.5.4 *Satellite cross-link system link budget for a* BER $= 10^{-12}$

As an example of free space pointing and tracking, this section calculates the link budget for a 10 Gbps NRZ OOK satellite cross-link communications system with 5 dB link margin. Assume we have constellation of communications satellites located in 800 km circular orbits with an approximate 100 min revisit time. Let us further assume the number of satellites allow us to have dynamic intersatellite ranges between 2600 km and 4600 km. Table 3 illustrates an example of the optimum link budget for a cross-link in the presence of jitter. This table shows the link can close with a better than 5 dB margin.

Assuming we want a high quality 10 Gbps communications link, then we need an average $R \cong 10^{-12}$, which implies an optimum θ_d/σ is 8.5751 from Table 1. (In the above table, both the probabilities P_F and P_S are specified to be 10^{-2}.) If the jitter equals 2.65 μrad, the beam divergence θ_d must be 23.3 μrad to obtain that value. This means that the pointing loss is -0.2 dB and the power penalty L_{pp} is -2.1 dB. Assuming we can close the link, what are our general pointing, tracking, and acquisition (PAT) requirements.

Residual radial pointing jitter on the order of <10% of the transmitter beam width (twice the beam divergence) delivers a received power versus time profile that supports reliable communications with an adequate average BER. To minimize random link BER degradation, the transmitting satellite must track the opposite platform with sub-microradian residual LOS jitter to keep the link's radial LOS pointing jitter around 4.6 μrad or less. A good ball-park estimate for the total root-sum-squared (RSS) static and dynamic terminal error contributions for the fine tracking mode would be about $1/3$ of the radial LOS pointing jitter, i.e., <1.5 μrad.

Acquisition (beacon) detection and handoff RSS terminal contributions nominally are 10's of mrad and a few mrad, respectively, which are less stressing. A complete system design is required to accurately specify all these parameters, but the above gives a reasonable estimate for the PAT requirements necessary to facilitate cross-link communications.

2.6 Electrical Signal-to-Noise Ratio in a Turbulent Channel

The turbulent channel range equation is a modification of the Friis range equation and is given as

$$P_{\text{rec}} \approx \gamma_{tx}\gamma_{rx}\gamma_{\text{fiber}} P_{tx} L_{\text{atm}} \left[\frac{A_{tx}A_{rx}}{(\lambda R)^2}\right] SR_{\text{RP}} SR_{\text{DP}} \approx \gamma_{rx}\gamma_{\text{fiber}} \langle I(0,R)\rangle A_{rx} SR_{\text{DP}}, \tag{72}$$

where

Table 3 Example of an optimum link budget estimated for space-to-space optical tracking and communications cross-link.

Parameter	Units	Tracking	Communications
TX power	Watts	1.000E+01	1.000E+01
TX power	dBm	4.000E+01	4.000E+01
Wavelength	Microns	1.550E-06	1.550E-06
TX aperture diameter =	Meters	6.656E-02	6.656E-02
TX aperture area	Meters-squared	3.479E-03	3.479E-03
TX transmittance	dB	−4.560E+00	−4.560E+00
Range =	Meters	4.600E+06	4.600E+06
RX aperture diameter	Meters	6.656E-02	6.656E-02
RX aperture area	Meters-squared	3.479E-03	3.479E-03
RX transmittance	dB	−2.000E+00	−2.000E+00
FSL =	dB	−6.623E+01	−6.623E+01
TX beam divergence	Radians	2.329E-05	2.329E-05
Sigma	Radians	2.600E-06	2.600E-06
Beam divergence/sigma	Unitless	8.957E+00	8.957E+00
Pointing loss	dB	−2.113E-01	−2.113E-01
Power penalty	dB	−2.099E+00	−2.099E+00
Received power	dBm	−3.510E+01	−3.510E+01
Rcvr sensitivity	dBm	−4.100E+01	−4.100E+01
Margin	dB	5.898E+00	5.898E+00
Fade level	dB	−1.027E+00	—
Surge level	dB	2.090E-01	—
Max/min range ratio-squared	dB	4.956E+00	—
Total dynamic range	dB	6.192E+00	—

$$\langle I(0,R)\rangle \approx \gamma_{tx} P_{tx} L_{\text{atm}} \left[\frac{A_{tx}}{(\lambda R)^2}\right] SR_{\text{RP}}, \tag{73}$$

is the average intensity at the receiver aperture. In the above equations,

$$L_{\text{atm}} = \int_0^R e^{-\alpha(h_0,\zeta) r(h_0,\zeta)} \mathrm{d}r, \tag{74}$$

$$\text{SR}_{\text{RP}} \approx \frac{1}{[1 + m(D_{tx}/r_{0\text{t}})^{5/3}]^{6/5}}, \quad m = \begin{cases} 1.000; \text{ with no AO}; & \sigma_I^2(0,R) > 1 \\ 0.280; \text{ with Tip/Tilt only}; & 0.1 \le \sigma_I^2(0,R) \le 1 \\ 0.052; \text{ with Full AO}; & \sigma_I^2(0,R) < 0.1 \end{cases}, \tag{75}$$

$$\text{SR}_{\text{DP}} \approx \frac{1}{[1 + m(D_{rx}/r_{0\text{r}})^{5/3}]^{6/5}}, \quad m = \begin{cases} 1.000; \text{ with no AO}; & \sigma_I^2(0,R) > 1 \\ 0.280; \text{ with Tip/Tilt only}; & 0.1 \le \sigma_I^2(0,R) \le 1 \\ 0.052; \text{ with Full AO}; & \sigma_I^2(0,R) < 0.1 \end{cases}, \tag{76}$$

$$r_{0rx} = \left[16.71\ \sec(\zeta) \int_0^R C_n^2(r)(r/R)^{5/3} \mathrm{d}r/\lambda^2\right]^{-3/5}, \tag{77}$$

and

$$r_{0tx} = \left[16.71\ \sec(\zeta) \int_0^R C_n^2(r)(1-r/R)^{5/3} \mathrm{d}r/\lambda^2\right]^{-3/5}, \tag{78}$$

where L_{atm} is the atmospheric loss; γ_{fiber} is the fiber coupling efficiency (EFC) (if applicable); ζ is the link zenith angle; r_{0rx} and r_{0tx} are the uplink spherical-wave Fried parameter for the receiver and transmitter, respectively;[27] and C_n^2 is the refractive index structure parameter.[9–11] The above equations for the Fried parameter are valid for $l_0 \ll r_0 \ll L_0$, with l_0 being the inner scale and L_0 being the outer scale of the turbulence. In Eq. (74), α is the volume extinction coefficient of the atmosphere, h_0 is the height above the ground. (Alternately, L_{atm} can be calculated using MODTRAN.[28]) The parameters SR_{RP} and SR_{DP} represent the Strehl ratio that is measured at the pupil plane of the receiver and the Strehl ratio that is measured at the detector plane of the receiver, respectively.[9–11] These parameters contain the new adaptive optics (AO) performance model that depends on the on-axis scintillation index $\sigma_I^2(0, R)$ or if the link range is short.[9–11] The scintillation index is the turbulent intensity variance given as

$$\sigma_I^2(r, R) = \frac{\langle I^2(r, R)\rangle}{\langle I(r, R)\rangle^2} - 1. \tag{79}$$

The parameter m in Eqs. (75) and (76) is a recognition that AO systems only work in weak turbulence or short ranges where phase fluctuations dominate but degrade in effectiveness as the turbulent channel migrates to moderate-to-strong turbulence levels where amplitude fluctuations dominate. Figure 12 shows the validity ranges of Eqs. (75) and (76) based on the experimental link budget comparisons in Ref. 12. For downlinks, the definitions in Eqs. (75) and (76) reverse. For horizontal links, the two Fried parameters are the same.

When the system uses an EDFA as a pre-detection amplifier, the received laser beam must be coupled into a single-mode fiber at the output of the receiver terminal. However, propagation through atmospheric turbulence degrades the spatial coherence of a laser beam and limits the fiber-coupling efficiency (FCE). That is, the turbulence affects the ability to focus the beam completely within the numerical aperture of the fiber. Dikmelik and Davidson[29] derived the following equation for the FCE under these conditions:

$$\gamma_{\text{fiber}} = 8a^2 \int_0^1 \int_0^1 e^{-(a^2 + A_{rx}/A_c)(x_1^2 + x_2^2)} I_0\left(\frac{A_{rx}}{A_c} x_1 x_2\right) x_1 x_2 \mathrm{d}x_1\, \mathrm{d}x_2, \tag{80}$$

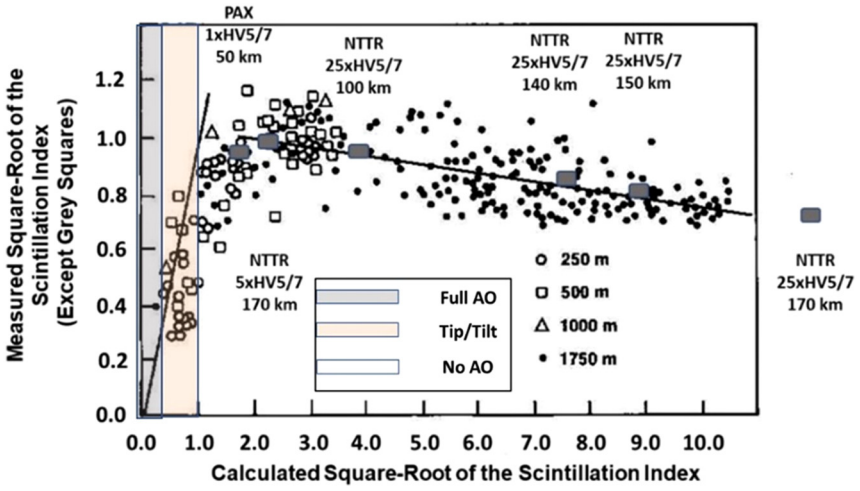

Fig. 12 Observed square-root of the scintillation index versus predicted square-root of the scintillation index plot with numbers from NTTR/PAX experiments showing the validity ranges of Eqs. (75) and (76).[12]

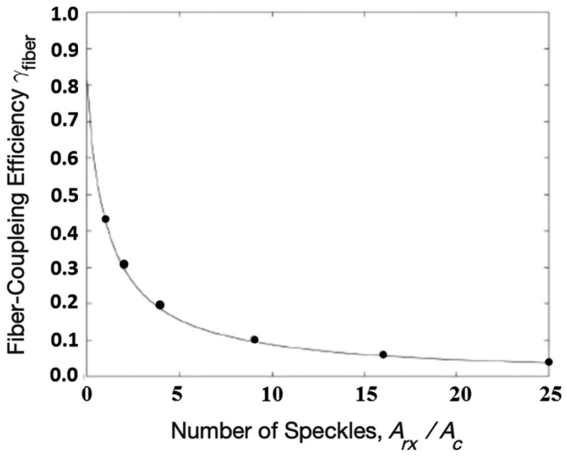

Fig. 13 FCE as a function of the number of speckles, A_{rx}/A_c, over the receiver aperture. The coupling parameter a equals 1.12 in this curve. The circles in this graph represent the coupling efficiency for optimized values of a derived for six specific number of speckles A_{rx}/A_c.

where γ_{fiber} is the FCE, a is the ratio of the receiver lens radius to the radius of the back propagated fiber mode, $A_{rx} = \pi D_{rx}^2/4$ is the area of the receiver aperture, D_{rx} is the diameter of the receiver aperture, and A_c is the spatial coherence area of the incident beam. In turbulence, the coherence area A_c essentially is the beam's speckle size, so the ratio A_R/A_c represents the number of speckles over the receiver aperture area.[29] To first order, the coherence area equals $A_c \simeq \pi r_0^2/4$.

In the absence of turbulence, the incident plane wave is fully coherent and the optimum value of a is 1.12.[29] Figure 13 depicts the FCE as a function of the number of speckles, A_{rx}/A_c, over the receiver aperture, with $a = 1.12$.

With turbulence, the optimum value of the coupling-geometry parameter a that maximizes the coupling efficiency depends on the value of the number of speckles A_R/A_c. Dikmelik and Davidson compared the coupling efficiencies for six optimum values with the efficiency calculated with the non-turbulence value.[29] Figure 13 also shows the resulting data points plotted with the $a = 1.12$ curve. This figure suggests that one can employ $a = 1.12$ for all FCE calculations with turbulence.

Following the procedure proposed by Andrews and Phillips (Ref. 9, pp. 459–460), the SNRs written in Eqs. (45) and (52) now are given as

$$Q = \frac{P_{\text{rec}}}{\sqrt{2qB_e[(P_{\text{rec}} + P_b)/R_\lambda + i_D/R_\lambda^2] + 4k_B T_0 B_e/G^2 R_\lambda^2 R_L + \sigma_I^2(0,R)P_{\text{rec}}^2}}, \tag{81}$$

and

$$Q \approx \frac{P_{\text{rec}}}{\sqrt{2h\nu N F_{\text{opt}} P_{\text{avg}} B_e + \sigma_I^2(0,R)P_{\text{rec}}^2}}, \tag{82}$$

respectively.

3 Electrical Signal-to-Noise Ratios in Coherent Optical Communications

This section will describe models for coherent optical communications.

3.1 Coherent Communications Receiver in Free Space

In a coherent beam detection system, the optical receiver beats its weak incoming (return) signal against a strong local oscillator (LO) signal to yield a more robust signal at the detector. Figure 14 shows a simplified layout of coherent laser communications receiver. The transmitted laser and LO beams interaction shift the incoming signal spectrum to an intermediate frequency (IF). This

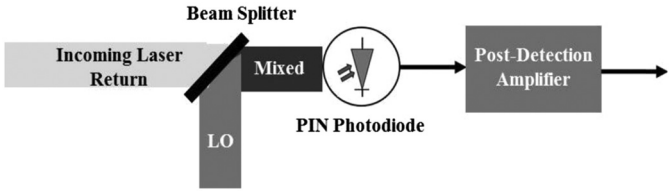

Fig. 14 Simplified schematic of a coherent laser communications receiver.

is known as heterodyne detection (homodyne detection shifts the incoming spectrum to baseband). The resulting signal is typically then sent to a transimpedance amplifier, followed by an IF filter and then a linear or square-law envelope detector. The dominant detection noise source for this receiver configuration is the LO shot noise.

In a heterodyne coherent detection system, the performance measure can be evaluated using either the carrier-to-noise ratio (CNR) at the IF filter output or the SNR at the low-pass filter (baseband) output at a secondary detector. The electrical SNR ($\mathrm{SNR_e}$) at a secondary detector equals

$$\mathrm{SNR_e^{coh}} = \frac{\Gamma^2(1+m/2)[{}_1F_1(-m/2;1;-\mathrm{CNR})-1]^2}{\Gamma(1+m)\,{}_1F_1(-m;1;-\mathrm{CNR})-\Gamma^2(1+m/2)\,{}_1F_1(-m/2;1;-\mathrm{CNR})}, \tag{83}$$

where $\Gamma(x)$ is the Gamma function and ${}_1F_1(a,b,c)$ is the confluent hypergeometric function.[30]

The parameter m can take on values of either 1 or 2 depending on whether we have a linear or square-law detector. For a linear rectifier, Eq. (83) does not reduce to a simple analytical equation but is close to the following expressions under large and small CNR limits:

$$\mathrm{SNR_e^{coh}}(1) \approx \frac{0.92\,\mathrm{CNR}^2}{1+0.46\,\mathrm{CNR}} = \begin{cases} 0.92\,\mathrm{CNR}^2; & \mathrm{CNR} \ll 1 \\ 2\,\mathrm{CNR}; & \mathrm{CNR} \gg 1 \end{cases}. \tag{84}$$

For a square-law detector, we have[30]

$$\mathrm{SNR_e^{coh}}(1) \approx \frac{\mathrm{CNR}^2}{1+2\,\mathrm{CNR}} = \begin{cases} \mathrm{CNR}^2; & \mathrm{CNR} \ll 1 \\ \mathrm{CNR}/2; & \mathrm{CNR} \gg 1 \end{cases}. \tag{85}$$

Figure 15 compares linear and square-law SNR as a function of CNR.[30] In the weak signal case, both detectors predict the output SNR to be roughly the square of the input CNR. Here, the signal is suppressed relative to the noise and both detectors behave like a quadratic rectifier. When the signal is strong prior to the envelope detector, the SNR at the output of each detector is proportional to the input CNR. That is, the contribution of the noise in this latter case is suppressed relative to the signal and both detectors behave like a linear system. For the remainder of this paper, we will assume a square-law envelope detector, but the analysis also is applicable to a linear detector.

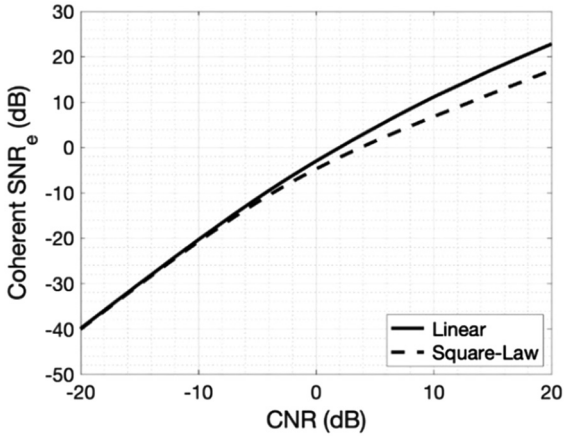

Fig. 15 Electrical SNR as a function of CNR for both linear and square-law envelope detectors.

3.2 Coherent Communications Receiver in Turbulence

In turbulence, Eq. (83) is still useful, but the CNR is modified for the degraded signal from the channel, and we include the turbulence-induced intensity variance. Specifically, we have

$$\mathrm{CNR} = \eta_{\mathrm{coh}} \eta P_{\mathrm{avg}} / (h_p \nu B_e) = 2\eta_{\mathrm{coh}} \mathrm{SNR}_{\mathrm{e}}^{\mathrm{QL}}, \tag{86}$$

and

$$\eta_{\mathrm{coh}} = \eta_{\mathrm{het}} \left[\frac{(1 + D_{rx}^2/4W_S^2)(1 + D_{rx}^2/4W_{\mathrm{LO}}^2)}{(1 + D_{rx}^2/8W_E^2) + (1 + D_{rx}^2/16F_E)^2} \right] \mathrm{MTF}_{\mathrm{turb}}, \tag{87}$$

where η_{het} is the heterodyne efficiency under perfect beam alignment. The bracketed term in Eq. (87) is the beam mismatch loss whose parameters are given as

$$\frac{1}{W_E^2} = \frac{1}{W_S^2} + \frac{1}{W_{\mathrm{LO}}^2}, \tag{88}$$

$$\frac{1}{F_E} = \frac{1}{F_s} + \frac{1}{F_{\mathrm{LO}}}, \tag{89}$$

and if an IF is needed

$$\varphi_{\mathrm{IF}} = kR - \varphi_{\mathrm{LO}} - \tan^{-1}\left(\frac{kD_{rx}^2/16F_E}{1 + D_{rx}^2/8W_E^2} \right), \tag{90}$$

where W_S and F_S are the incoming signal intensity beam radius and phase front radius of curvature, respectively, W_{LO} and F_{LO} are the LO intensity beam radius and phase front radius of curvature, respectively, and φ_{IF} and φ_{LO} are the IF and LO longitudinal phases, respectively. It is often used as a measure of detector performance because it measures the loss in coherent power that arises when the received field and the LO are not perfectly matched. If the LO characteristics match those of the incoming signal, which means $W_{\mathrm{LO}}^2 = W_S^2$, $F_{\mathrm{LO}} = F_S$, and $\varphi_{\mathrm{LO}} = kR$, $F_E = \infty$, and $W_E^2 = W_S^2/2$, then the heterodyne efficiency is η_{het}, which is its maximum value. Otherwise, there will be some additional loss besides η_{het}. In Eq. (87), the modulation transfer function (MTF) for the turbulent channel equals

$$\mathrm{MTF}_{\mathrm{turb}} = \eta_{\mathrm{het}}^{\mathrm{turb}} = \int_0^1 u e^{-3.443(uD_{rx}/r_0)5/3} \mathrm{d}u. \tag{91}$$

Figure 16(a) shows $\eta_{\mathrm{het}}^{\mathrm{turb}}/\eta_{\mathrm{het}}$ as a function of D_{rx}/r_0. To get good mixing efficiency and minimize Strehl ratio losses, the receiver aperture diameter must be less than the Fried parameter at the receiver, e.g., for a 75% normalized heterodyne efficiency, one needs $D_{rx} \approx 0.5 r_0$.

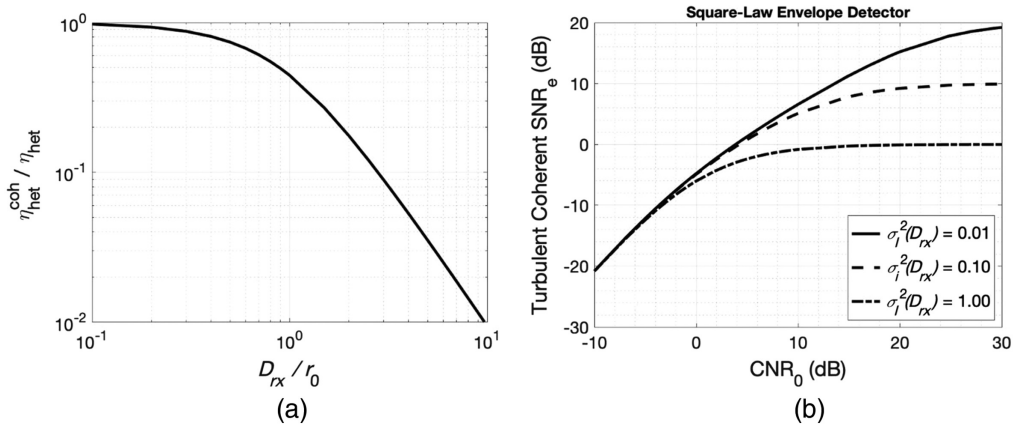

Fig. 16 Graph of (a) the normalized heterodyne efficiency as function of and (b) the turbulent coherent SNR as a function of the turbulent CNR for a three beam-wander intensity scintillation ratio.

In Eq. (86), $\mathrm{SNR}_e^{\mathrm{QL}}$ is the quantum-limited SNR given as

$$\mathrm{SNR}_e^{\mathrm{QL}} \approx \frac{\eta P_{\mathrm{avg}}}{2h_p \nu B_e}, \tag{92}$$

where η is the detector quantum efficiency, P_{avg} is the averaged received signal power, h_p is Planck's constant, $\nu = c_0/\lambda$ is the laser frequency, c_0 is the speed of light in vacuum, λ is the laser wavelength, and B_e is the baseband bandwidth derived from the lowpass filtering after the envelope detector.

In turbulence, the coherent electrical SNR at the lowpass output of a square-law detector is written as[30]

$$\mathrm{SNR}_e^{\mathrm{coh}}(2) = \frac{\mathrm{CNR}^2}{1 + 2\,\mathrm{CNR} + \sigma_I^2(D_{rx})\mathrm{CNR}^2}. \tag{93}$$

Figure 16(b) shows the turbulent coherent SNR as a function of the turbulent CNR for three beam-wander intensity scintillation ratios. Here, $\mathrm{CNR}_0 = 2\eta_{\mathrm{het}}^{\mathrm{turb}}\mathrm{SNR}_e^{\mathrm{QL}}$. This chart shows that the scintillation indices create constant SNRs for large CNR_0, which in turn will generate constant BER curves. This suggests that other means for turbulence mitigation must be used to get the BER down to reasonable levels. However, this is the only issue with a coherent system approach in the turbulent channel. Achieving a high turbulent CNR is hard because the phase perturbations in the received signal's phase front do not mix well with the LO's phase front.

4 Channel Models

Although there are many refractive index structure parameter models in the literature, there are two models that are most popular within the optics community. One is the Hufnagle–Valley (HV5/7) model and the other is the Hufnagle–Andrews–Phillips (HAP) model. This section will summarize both models, as well as present the round-earth model for those situations where the curvature of the earth affects the link analysis.

4.1 Refractive Index Structure Parameter Models

There are two refractive index structure parameter models used most often by the community. One is the Hufnagel-Valley 5/7 C_n^2 model, which is called the 1xHV5/7 model because for $\lambda = 0.5$ μm and $\zeta = 0$ deg, it predicts a 5 cm Fried parameter and 7 μrad isoplanatic angle. Mathematically, it is written as

$$C_n^2(h) = M\left\{\begin{array}{l} 0.00594\left(\frac{w}{27}\right)^2\left(\frac{h}{10^5}\right)^{10}\exp\left(-\frac{h}{1000}\right) \\ +2.7\times 10^{-16}\exp\left(-\frac{h}{1500}\right) + C_n^2(0)\exp\left(-\frac{h}{100}\right)\end{array}\right\}, \tag{94}$$

with M being a scaling to represent the strength of the average high altitude background turbulence $C_n^2(0) = 1.7\times 10^{-14}$ m$^{-2/3}$.[9–11] This allows the model to be used when $C_n^2(0)$ are not available. (As it turns out, $M \times C_n^2(0)$ usually turns out to be close to the measured ground value.[31]) It has long been recognized that the advantage of this model over other atmospheric models is its inclusion of the rms wind speed, w, and the ground level refractive index structure parameter. Their inclusion permits variations in high-altitude wind speed and local near-ground turbulence conditions to better model real-world profiles over an extensive range of geographic locations. It also provides a model consistent with measurements of the Fried parameter r_0 and the isoplanatic angle θ_0. Let us see an example on how it is used.

Takenaka et al. reported some fiber coupling experimental result using the old version of the HV5/7 equation (Ref. 10, p. 100), a slew rate of 0.35 deg/s, and ground refractive index structure parameter of 1×10^{-13} m$^{-2/3}$.[32] The source of some of their parameters like the average wind speed of 88 m/s was Ref. 33. Figure 17 exhibits their EFC measurements (blue data) with their estimate of EFC, −17 dB, (red-dashed line) using this HV5/7 model and their evaluation of Eq. (64) using

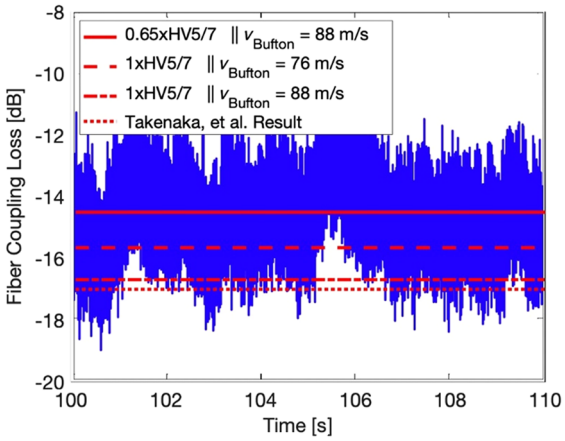

Fig. 17 EFC measurements with various analytical EFC estimates.

$$a = \frac{\pi D_{rx} W_m}{2\lambda F_0}, \tag{95}$$

where W_m is the fiber-mode field radius at the fiber end face and F_0 is the receiver focal length. Now, the cited ground refractive index structure parameter for ground site is 2.68×10^{-14} $\mathrm{m}^{-2/3}$, which is the reported value of that site's mean nighttime $C_n^2(0)$.[34] The International Telecommunication Union (ITU) recommends the 1xHV5/7 model for the nighttime operations analyses.[35] Using Eq. (80) with $a = 1.12$, the 1xHV5/7 model and the receiver Fried parameter, one obtains an EFC estimate of -16.69 dB (red-dash-dot line), which is a slightly better estimate of the EFC measurements than the Takenaka et al. result. If one uses the average wind speed of 76 m/s used by Ref. 34, then one obtains a better EFC estimate of -15.65 dB (red-dash line). On the other hand, if one uses 0.65xHV5/7 and an average wind speed of 88 m/s, one calculates a very good EFC estimate of -14.5 dB (red-solid line). The importance of this example is to show that measuring the refractive index structure parameter vertical profile via some method like radiosonde, or at least measuring the ground refractive index structure parameter, may provide better accuracy in link analyses.

Equation (93) has a slowly decreasing exponential term with altitude.[13,31] This conflicts with the $C_n^2(h)$ behavior of $h^{-4/3}$ noted by Walters and Kunkel[36] and supported by several other early measurements. To better represent this trend, Stotts and Andrews modified the HAP model to yield

$$C_n^2(h) = M\left[1.04 \times 10^{-3}\left(\frac{w}{27\,m/s}\right)^2\left(\frac{h+h_G}{10^5\,m}\right)^{10}\exp\left(-\frac{h+h_G}{1200\,m}\right) + 2.7 \times 10^{-16}\exp\left(-\frac{h+h_G}{1700\,m}\right)\right] + C_n^2(h_G)\left(\frac{h_G}{h}\right)^{4/3}, \quad h > h_G, \tag{96}$$

in units of $\mathrm{m}^{-2/3}$, where $h_G = 5$ m always.[37] This model is referred to as the modified HAP model. For the first few hundred meters, there is considerable difference between these two models. However, at $\sim$1 km and higher altitudes, the models are essentially the same with $M = 1$ and same $C_n^2(0)$. Equation (96) also is the more appropriate model for optical links close to the ground. To account for various times of the day, the 4/3 power law in the last term can be replaced by a variable power p as described on p. 101 of Ref. 10.

Figure 18 shows a comparison between Eq. (96), evaluated at specific M and $C_n^2(h_0)$ values, and the annual Korean $C_n^2(h)$ profiles at the 1%, 15%, 50%, 85%, and 99% cumulative percentiles.[38] The latter data come from an Air Force Research Laboratory's data base of 85 radiosonde balloon flights over South Korea. This graph shows good agreement between the theory and data. Let us see how this model compares with a typical refractive index structure parameter vertical profile.

Figure 19 depicts Eq. (96) with $C_n^2(h_0) = 1 \times 10^{-14}$ $\mathrm{m}^{-2/3}$, $M = 0.7$, and $h_0 = 1$ m against the mean of the $C_n^2(h)$ measurements obtained at the Teide Observatory (OT) during 2004 (dotted

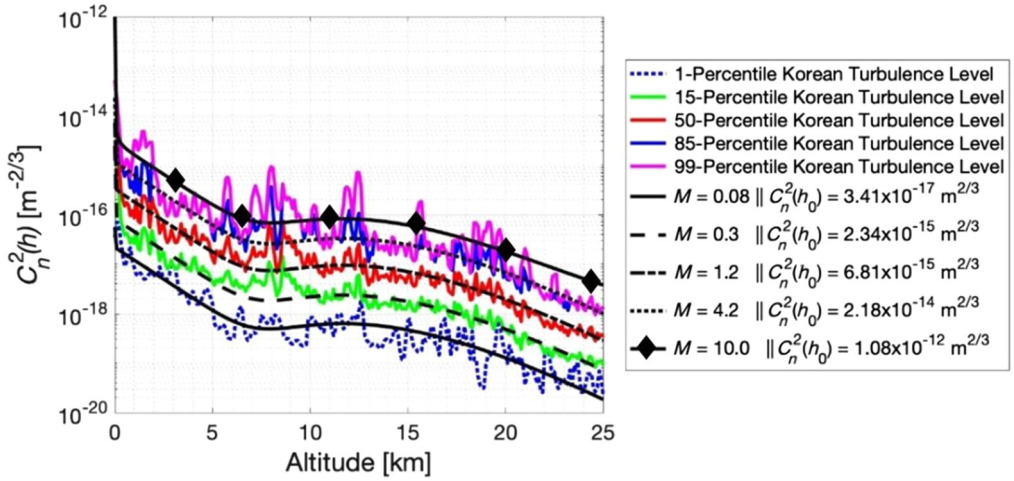

Fig. 18 Comparison between Eq. (96) evaluated at specific M and $C_n^2(h_0)$ values and the annual Korean $C_n^2(h)$ profiles at the 1%, 15%, 50%, 85%, and 99% cumulative percentiles.[38]

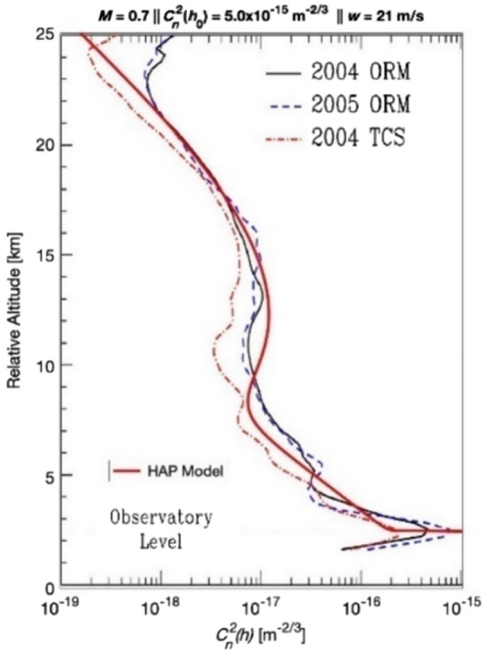

Fig. 19 Comparison between Eq. (96) and the mean of the measurements obtained at the Teide Observatory (OT) during 2004 (dotted-shorted line) and at the Roque de los Muchachos Observatory (ORM) during 2004 (solid line) and 2005 (dashed line).[39] (Data used with permission of Dr. Julio A. Castro-Almazán and Dr. Begoña García-Lorenzo.)

- shorted line) and at the Roque de los Muchachos Observatory (ORM) during 2004 (solid line) and 2005 (dashed line).[39] The horizontal line indicates the observatory altitude (2400 m). These statistical profiles correspond to the weighted average of the individual monthly statistical profiles. The number of individual profiles measured each month was used as weights.[39] These data were derived from the Scintillation Detection and Ranging (SCIDAR) procedure.[39] This technique is based on the statistical analysis of scintillation patterns produced at a telescope pupil by the light from two stars of a binary system. The profiles of the refractive index structure parameter come from the inversion of the average normalized autocovariance of many patterns. We see reasonable agreement between theory and data. Reference 37 showed other reasonable comparisons.

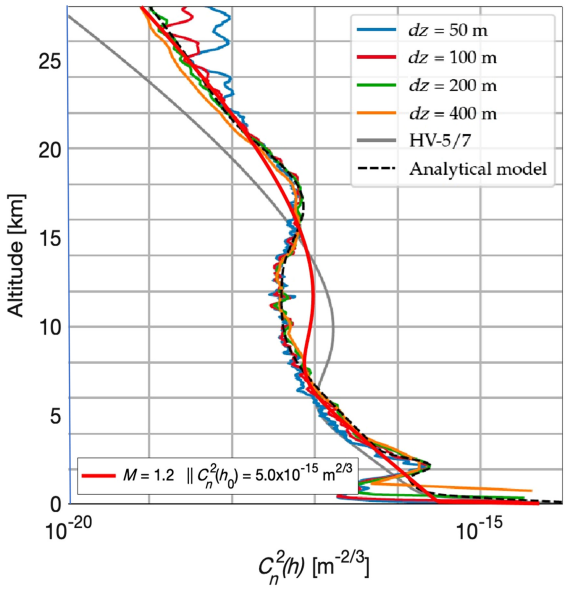

Fig. 20 Plots of the refractive index structure parameter versus altitude estimates derived from data taken at Hilo, Hawaii, and curves generated from the 1xHV5/7 model, a specific analytical mode and Eq. (94).[40] (Data used with permission of Mr. Florian Quatresooz and Professor Claude Oestges.]

Figure 20 shows a year-long average of the refractive index structure parameter profile versus altitude estimates as a function of the re-interpolation distance dz (estimate's vertical spacing) generated by Quatresooz et al., using the high-density profiles from the University of Wyoming (UWYO) Atmospheric Science Radiosonde Archive.[40] This set of data profiles is for Hilo, Hawaii. Besides the data curves, curves generated from the 1xHV5/7 $C_n^2(h)$ model, a curve-fit model they created, denoted as analytical model in the figure, and the above modified HAP model for $M = 1.2$ and $C_n^2(h_0) = 5 \times 10^{-15}$ m$^{-2/3}$. Again, the modified HAP model does a pretty good job in following most of the averaged data well just using a two-parameter fit. It does not follow the nominal 12-km bump very well, but it does follow the upper and lower atmosphere profiles much better than the HV5/7 model does.

Mahmood et al. suggested that $C_n^2(h)$ comparisons with experimental data can be improved by using their associated wind speed profiles with altitude via the turbulent intensity.[41] To evaluate this premise, we modify Eq. (96) to be

$$C_n^2(h) = M\left[1.04 \times 10^{-3}\left(\frac{9\,m/s}{w\left(h+h_g\right)}\right)^2\left(\frac{h+h_G}{10^5\,m}\right)^{10}\exp\left(-\frac{h+h_G}{1200\,m}\right)\right.$$
$$\left. + 2.7 \times 10^{-16}\exp\left(-\frac{h+h_G}{1700\,m}\right)\right] + C_n^2(h_0)\left(\frac{h_0}{h}\right)^{4/3},\ h > h_0 > h_G, \tag{97}$$

to reflect a turbulent intensity with a wind speed profile dependence, where $w(h)$ is the associated wind speed vertical profile. Figure 21 compares Eq. (97) with Hilo (dz = 200 m)-$C_n^2(h)$ using that wind speed profile supplied by Mr. Quatresooz and Professor Oestges.[40] The two profiles are in better agreement in the 12-km and upper region but deviate some in the lower atmospheric region. However, both figures are in reasonable agreement with the data overall.

4.2 Round Earth Model

Many satellite laser communications analyses are performed using the above refractive index structure parameter vertical profile models and a flat-earth model in which the curvature of the Earth is ignored. For small zenith angles, this model works well. However, for larger zenith angles, the curvature of the earth must be considered. Assuming the Earth is a sphere, the altitude h above the ground reference point h_0 at a zenith angle ζ is described as

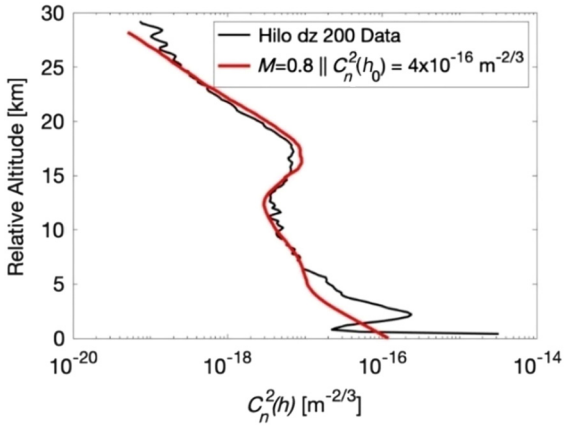

Fig. 21 Plots of the refractive index structure parameter versus altitude measurements (Hilo, Hawaii), and Eq. (97) using the wind speed profile provided by Mr. Quatresooz and Professor Oestges[40] (data used with their permission).

$$h(z) = \sqrt{(R_E + h_0)^2 + 2z(R_E + h_0)\cos(\zeta) + z^2} - (R_E + h_0) + h_G, \tag{98}$$

for $h > h_0$, where $R_E = 6371$ km (Ref. 10, p. 112).

5 Communications Bit Error Rate Equations and the Probability of Fade

This section will present the BER equations for most popular signaling formats in free space optical communications (FSOC) as well as the probability of fade equation, which is just $P_{\text{fade}} = 1 - P_d$, where P_d is the probability of detection. We then will discuss now these equations in analyzing FSOC in turbulence.

5.1 BER in Free Space

Table 4 summarizes the BER equations for the most popular signaling formats for FSOC. In the MPPM line, the parameter M equals 2^{k_b} where k_b is the number bits per laser pulse.

5.2 BER and Probability of Fade in Turbulence

Figure 22 shows typical power in the fiber (PIF) (blue curve) and power out of the fiber (POF) (green curve) signals and their respective PDFs measured over a 183-km, NRZ OOK communications link cited taken at 01:52 UTC on May 18, 2009, at the Nevada Test and Training Range (NTTR).[7] (This figure also shows the fielded system had 2 dB higher gain at low PIF than the system measured in the lab caused by minor system upgrade prior to field test.)

Link budgets generally use the 50-percentile received signal power, which is either the average received power for symmetric intensity PDF or the median received power for non-symmetric intensity PDFs. In turbulent conditions, the calcuated signal is the latter. Figure 23 shows the cummulative density function for the received PIF power derived from tests cited in.[7] The PIF looks like it is log-normal. These figures indicate that the received signals are above the median 50% of the time and below the median for 50% of the time. It does not show that the higher received signals above the median are sufficient to be called a "1." Turbulence mitigation must be employed to get the received signal to be above the threshold for a "1," which is shown in Fig. 22 by those used to create the POF.[7]

To calculate the link availability, one generally uses the fade margin equation, which accounts for the additional power needed to overcome link fading. The basic form of the fade margin equation in free space is

$$\begin{aligned}\text{Fade Margin (dB)} = {} & \text{System Margin (dB)} + P_{tx}\,(\text{dBm}) \\ & - \gamma_{tx}\,(\text{dB}) - \gamma_{rx}\,(\text{dB}) - \text{FSL (dB)} - P_{avg}^{\min}\,(\text{dBm}).\end{aligned} \tag{99}$$

Table 4 Most popular FSOC signaling formats and their BER equations.

Signaling format	BER
Non-return to zero on-off keying (NRZ-OOK)[3,31]	$\mathrm{BER}_{\mathrm{NRZ-OOK}} = 0.5\,\mathrm{erfc}\left(\sqrt{\mathrm{SNR}_e}/2\sqrt{2}\right)$
Return to zero on-off keying (RZ-OOK)[3]	$\mathrm{BER}_{\mathrm{RZ-OOK}} = 0.5\,\mathrm{erfc}\left(\sqrt{\mathrm{SNR}_e}/\sqrt{2}\right)$
Differential phase shift keying (DPSK)[3]	$\mathrm{BER}_{\mathrm{DPSK}} = 0.5\,\mathrm{erfc}\left(\sqrt{\mathrm{SNR}_e}/\sqrt{2}\right)$
M-ary pulse position modulation (MPPM) (Ref. 21, p. 197)	$\mathrm{BER}_{\mathrm{MPPM}} = \left(\frac{M/2}{M-1}\right)\left[1-\frac{1}{\sqrt{2\pi}}\int_{-\infty}^{\infty} e^{-\left(x-\sqrt{\mathrm{SNR}_e}\right)^2/2}\left(1-0.5\,\mathrm{erfc}\left(x/\sqrt{2}\right)\right)^{M-1}\mathrm{d}x\right]$
Binary pulse position modulation (Ref. 21, p. 197)	$\mathrm{BER}_{\mathrm{BPPM}} \approx 0.5\,\mathrm{erfc}\left(\sqrt{\mathrm{SNR}_e}/2\right) \le \mathrm{BER}_{\mathrm{MPPM}}$
Binary phase shift keying[1]	$\mathrm{BER}_{\mathrm{BPSK}} = 0.5\,\mathrm{erfc}\left(\sqrt{\mathrm{SNR}_e}\right)$

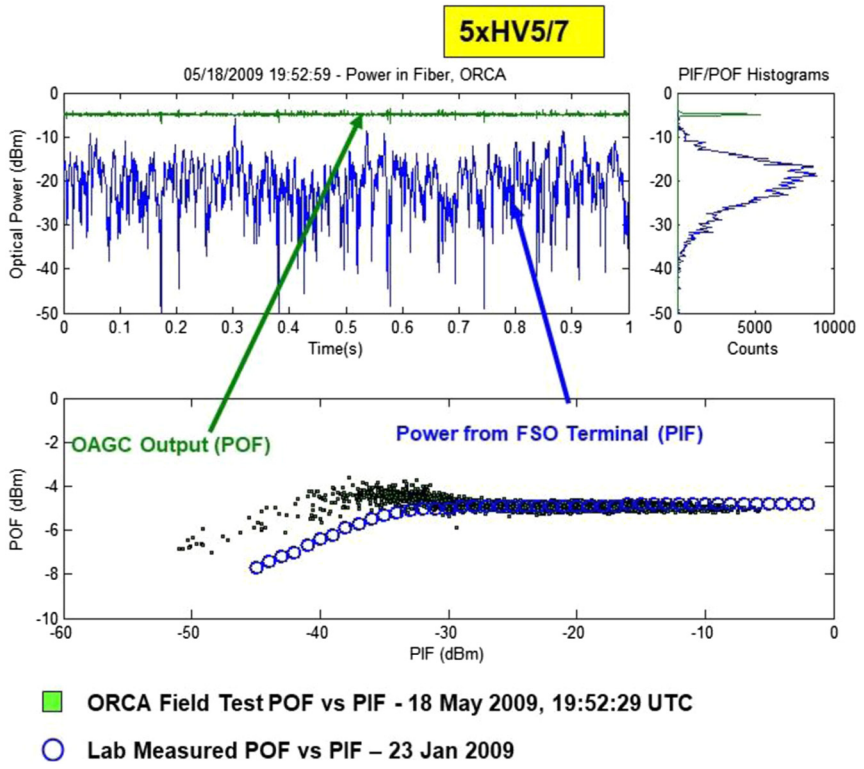

Fig. 22 Typical display of the received PIF and POF signals and their respective PDFs derived from 183-km NRZ OOK optical communications link under 5xHV5/7 turbulence conditions.[7]

This implies that the probability of detection is given as

$$P_d = 0.5\,erfc\left[(\text{fade margin-OSNR})/2\right] = 0.5\,erfc[(\text{system margin})/\sqrt{2}\,], \tag{100}$$

and the probability of fade, which is the percentage of time the received intensity is below a prescribed threshold value, equals

$$P_{\text{fade}} = 1 - P_d = 1 - 0.5\,erfc\left[(\text{system margin})/\sqrt{2}\,\right]. \tag{101}$$

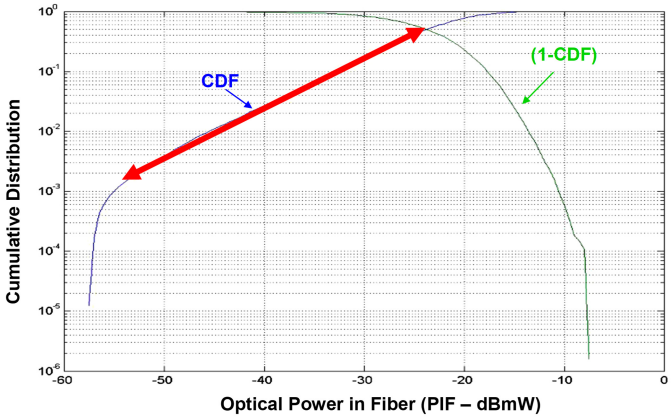

Fig. 23 The statistical distribution of the PIF produces a consistent linear relationship between log optical power and log cumulative distribution.[7]

For zero margin, we have

$$P_{\text{fade}} = 1 - P_d = 1 - 0.5erfc[0] = 0.5,$$

which is expected as OSNR represents the average (50% level) optical SNR as noted earlier.

Let us now turn to the BER. The unconditional BER in the presence of turbulence-induced scintillation should be averaged with respect to the turbulence-induced intensity PDF to yield the average BER for those conditions. Specifically, we write

$$\overline{\text{BER}} = \int_0^\infty p_I(I')\text{BER}(I')\text{d}I';\ I' > 0 \tag{102}$$

using the appropriate BER equation for the signaling format utilized and a scintillation index appropriate for the link's turbulence and geometry conditions. In many cases, the log-normal (LN) PDF is used in Eq. (102), which is given as

$$p_{\ln I}(I') = \frac{1}{I'\sqrt{2\pi\sigma^2_{\ln I}(D_{rx})}}\ \exp\left\{-\frac{[\ln(I') + 0.5\sigma^2_{\ln I}(D_{rx})]^2}{2\sigma^2_{\ln I}(D_{rx})}\right\}, \tag{103}$$

with $\sigma^2_{\ln I}(D_{rx}) = \ln[1 + \sigma^2_I(D_{rx})]$, which is valid in the weak-to-moderate intensity fluctuations regimes when the receiver aperture is large (Ref. 10, p. 94). The alternative is to replace $p_{\ln I}(I')$ in Eq. (102) by the Gamma–Gamma (GG) PDF that is written as

$$p_I(I') = \frac{2(\alpha\beta)^{(\alpha+\beta)/2}}{\Gamma(\alpha)\Gamma(\beta)}(I')^{(\alpha+\beta)/2-1}K_{\alpha-\beta}\left(2\sqrt{\alpha\beta I'}\right), \tag{104}$$

where $K_\nu(x)$ is the modified Bessel function of the second kind,

$$\alpha = \frac{1}{\sigma^2_X(D_{rx})} \tag{105}$$

and

$$\beta = \frac{1}{\sigma^2_Y(D_{rx})} \tag{106}$$

with $\sigma^2_X(D_{rx})$ being the large-scale intensity variance and $\sigma^2_Y(D_{rx})$ being the small-scale intensity variance (Ref. 10, p. 94).

Equation (104) is valid in the weak-to-strong intensity fluctuations regimes when the receiver aperture is small as well as with certain large values of D_{rx}. Experimental and computer simulation results indicate that Eq. (103) may be valid in deep turbulence when $D_{rx} < \rho_0$ or when $D_{rx} > R/k\rho_0$ with $\rho_0 = r_0/2.1$ being the lateral spatial coherence radius. For apertures sizes between these extremes, Eq. (103) may be the better model (Ref. 10, p. 94).

As was suggested by one of the reviewers, we need to note that a specific PDF model valid for all turbulence conditions is still an open question, particularly after going through a receiver aperture. That is, which PDF tails are correct. This was investigated in chapter 5 of Ref. 11.

6 Scintillation Indices for Various Link Geometries

Fluctuations in the received signal intensity resulting from the propagation through turbulent channel is commonly described as "scintillation." The term scintillation includes the temporal variation of received intensity (such as star twinkling) and spatial variation within a receiver aperture (such as speckle). Its magnitude is link-geometry dependent.

This section will present the scintillation indices for uplink, downlink, and horizontal communications link geometries.

6.1 Uplink Communications Scintillation Indices and PDFs

In uplink communications geometry, a large beam will be incident on the satellite receiver aperture from diffraction and turbulent beam spreading. Beam wander will be several microradians and will create additional scintillation at the receiver, dependent on transmitter beam size. Angle of arrival fluctuations is typically less than a microradian. Aperture averaging cannot be used as the speckle/Fried parameter will be much larger than the receiver diameter. (Note that multiple beams through statistically independent atmospheric paths can reduce scintillation as a kind of aperture averaging, if available.) This means one now has scintillation at the receiver caused by beam wander. Specifically, the turbulence near the Earth's surface causes a lever-arm effect at the satellite, causing signal intensity to occur. This means that tip/tilt ($N = 3$ Zernike modes) tracking is necessary to reduce beam-wander scintillation. Specifically, we now need a beam-wander intensity PDF that considers whether the incoming beam is tracked or not.

Uplink beam wander has a significant effect on laser communications link performance. This requires tracked/tilt-corrected and untracked beam wander models.[40] The key to these models is two sets of nondimensional beam parameters—one set at the transmitter and a second set at the receiver at distance R. For collimated transmitter, we have

$$z = 0\colon\ \Theta_0 = 1 - \frac{R}{f_{\mathrm{FL}}} = 1, \quad \Lambda_0 = \frac{2R}{kW_0^2} = \frac{8\lambda R}{\pi D_{tx}^2}, \tag{107}$$

whereas at the receiver, the corresponding beam parameters are

$$z = R\colon \begin{cases} \Theta = \frac{\Theta_0}{\Theta_0^2 + \Lambda_0^2}, \\ \overline{\Theta} = 1 - \Theta, \\ \Lambda = \frac{\Lambda_0}{\Theta_0^2 + \Lambda_0^2} = \frac{2R}{kW^2} = \frac{\lambda R}{\pi W^2} \end{cases}. \tag{108}$$

In the above equations, $\Theta_0 = 1 - R/f_{\mathrm{FL}}$ describes the amplitude change due to refraction of focusing, Λ_0 describes the amplitude change due to aperture diffraction, $k = 2\pi/\lambda$, W_0 is the e^{-2}-intensity beam radius, and (Ref. 10, p. 18–19)

$$W = W_0\sqrt{\Theta_0^2 + \Lambda_0^2} = \sqrt{\frac{\lambda R}{\pi \Lambda}}. \tag{109}$$

When $D_{tx}/r_{0t} \ll 1$ or $D_{tx}/r_{0t} \gg 1$ beam tracking is not necessary and the associated PDF for the incoming intensity ($\propto$ power in the bucket [PIB]) is just a simple Gamma (G) distribution:

$$p_I(I)dI = \frac{1}{\Gamma(m_0)I}\left[\frac{m_0 I}{\langle I(0,R)\rangle}\right]^m \exp\left\{-\frac{m_0 I}{\langle I(0,R)\rangle}\right\}\mathrm{d}I, \ I > 0, \tag{110}$$

or

$$p_I(I')dI' = \frac{1}{\Gamma(m_0)I'}[m_0 I']^m \exp\{-m_0 I'\}\mathrm{d}I', \quad I' > 0, \tag{111}$$

where the shape parameter $m_0 = 1/\sigma_{I,l}^2(0,R)_{\text{Tracked}}$, $\sigma_{I,l}^2(0,R)$ is the on-axis scintillation index, and $I' = I/\langle I(0,R)\rangle$ (Ref. 10, p. 113).

When $1 < D_{tx}/r_{0t} < 10$, beam wander-induced scintillation becomes important, and the beam probability needs to be tracked. If the beam is tracked, then Eq. (110) or Eq. (111) is used with tilt-corrected m_0. If the beam is not tracked, the resulting PDF distribution can be modeled as a modulated gamma distribution (MG), which is given as

$$p_I^u(I)dI = \frac{\vartheta}{\Gamma(m_1)I}\left(\frac{m_1 I}{(1+1/\vartheta)\langle I(0,R)\rangle}\right)^{\vartheta}\Gamma\left(m-\zeta,\frac{m_1 I}{(1+1/\vartheta)\langle I(0,R)\rangle}\right)dI, \tag{112}$$

or

$$p_I^u(I')dI' = \frac{\vartheta}{\Gamma(m_1)I'}\left(\frac{m_1 I'}{(1+1/\vartheta)}\right)^{\vartheta}\Gamma\left(m_1-\zeta,\frac{m_1 I'}{(1+1/\vartheta)}\right)dI', \tag{113}$$

where $\Gamma(x,a)$ is the incomplete Gamma function, $m_1 = 1/\sigma_{I,l}^2(0,L)_{\text{untracked}}$ is the distribution's shape parameter (Ref. 10, p. 113). In Eqs. (112) and (113), we have

$$\vartheta = \sqrt{1+\frac{1+\sigma_{I,l}^2(0,R)_{\text{untracked}}}{34.29(\Lambda R/kr_{0T}^2)^{5/6}(\sigma_{pe}^2/W^2)}} - 1, \tag{114}$$

where

$$\sigma_{pe}^2 = \langle r_c^2\rangle\left[1-\left(\frac{\pi^2\left[D_{tx}/\left(2\sqrt{2}r_{0t}\right)\right]^2}{1+\pi^2\left[D_{tx}/\left(2\sqrt{2}r_{0t}\right)\right]^2}\right)^{1/6}\right], \tag{115}$$

with

$$\langle r_c^2\rangle = \left[\frac{7.25(R-z_0)^2}{[D_{tx}/2^{3/2}]^{1/3}}\right]\int_{z_0}^{R} C_n^2(h)\left[1-\frac{z-z_0}{R-z_0}\right]^2 \mathrm{d}z, \tag{116}$$

with $R - z_0 = (H-h_0)/\cos\,\xi$, H is the satellite altitude, and $z - z_0 = (h-h_0)/\cos\,\xi$ (Ref. 10, pp. 109–113). In the case of a collimated beam, Eq. (116) becomes

$$\langle r_c^2\rangle = 0.54\left[\frac{\lambda R}{D_{tx}/\sqrt{2}}\right]^2\left(\frac{D_{tx}/\sqrt{2}}{r_{0t}}\right)^{5/3}. \tag{117}$$

The untracked on-axis scintillation index equals

$$\sigma_{I,l}^2(0,R)_{\text{untracked}} = 34.29\left(\frac{\Lambda R}{kr_{0\ t}^2}\right)^{5/6}\left[\frac{\sigma_{pe}^2}{D_{tx}^2/8}\right] + \exp\left\{\frac{0.49\sigma_{\text{Bu}}^2}{[1+0.56(1+\Theta)\sigma_{\text{Bu}}^{12/5}]^{7/6}}+\frac{0.51\sigma_{\text{Bu}}^2}{[1+0.69\sigma_{\text{Bu}}^{12/5}]^{5/6}}\right\}-1, \tag{118}$$

where

$$\sigma_{\text{Bu}}^2 = 8.70k^{7/6}(H-h_0)^{5/6}\sec^{11/6}(\zeta)\text{Re}\left\{\int_{h_0}^{H} C_n^2(h)[\xi^{5/6}(\Lambda\xi + i(1-\overline{\Theta}\xi))^{5/6} - \Lambda^{5/6}\xi^{5/3}]\mathrm{d}h\right\}, \tag{119}$$

$$\xi = 1-(h-h_0)/(H-h_0), \tag{120}$$

with $\overline{\Theta} = 1-\Theta$ (Ref. 10, p. 110).

The tip/tilt-corrected on-axis scintillation index equals

$$\sigma_{I,l}^2(0,R)_{\text{tracked}} = 34.29\left(\frac{\Lambda R}{kr_{0t}^2}\right)^{5/6}\left[\frac{\sigma_{pe-TT}^2}{D_{tx}^2/8}\right] + \exp\left\{\frac{0.49\sigma_{\text{Bu}}^2}{[1+0.56(1+\Theta)\sigma_{\text{Bu}}^{12/5}]^{7/6}}+\frac{0.51\sigma_{\text{Bu}}^2}{[1+0.69\sigma_{\text{Bu}}^{12/5}]^{5/6}}\right\}, \tag{121}$$

where

$$\sigma_{pe-TT}^2 = \left[\sqrt{\langle r_c^2 \rangle} - T_z R\right]^2 \left[1 - \left(\frac{\pi^2 \left[D_{tx}/\left(2\sqrt{2}r_{0t}\right)\right]^2}{1 + \pi^2 \left[D_{tx}/\left(2\sqrt{2}r_{0t}\right)\right]^2}\right)^{1/6}\right], \tag{122}$$

and (Ref. 10, pp. 109–110)

$$T_z = 0.57\left(\frac{\lambda}{D_{tx}/\sqrt{2}}\right)\left(\frac{D_{tx}/\sqrt{2}}{r_{0t}}\right)^{5/6}. \tag{123}$$

The on-axis scintillation index for both tracked and untracked beams is shown in Fig. 24 as a function of beam radius W_0 along with computer simulation data.[42] The tracked results are tip/tilt-corrected based on Eq. (121), whereas the untracked results come from Eq. (118). The computer simulation data and theoretical results are based on the 1xHV-5/7 profile model and $\zeta = 0$ deg. The agreement between theoretical and simulation results is good.

Figure 25 plots the on-axis scintillation index of an untracked 0.84-μm beam as a function of beam size at two zenith angles (0 deg and 60 deg) along with the Rytov theory result at 0 deg zenith angle. Computer simulation data were taken at geostationary orbit (GEO), so here we chose the larger scaling constant 3.86 instead of π in Eq. (115) for a slightly better fit at GEO. Again, the agreement between theoretical and simulation results is good.

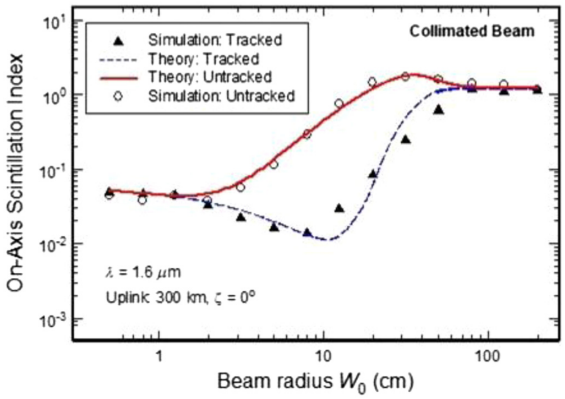

Fig. 24 On-axis scintillation index for both tracked (tilt-corrected) and untracked collimated beams to LEO as a function of beam radius (simulation results courtesy of G. J. Baker[42]).

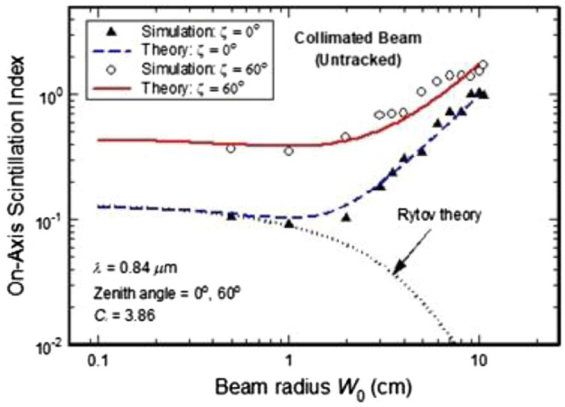

Fig. 25 On-axis scintillation index at GEO for an untracked beam with zenith angles of 0 deg and 60 deg as a function of beam radius. The dotted curve is Rytov theory at 0 deg zenith. The 1xHV-5/7 and flat-Earth models were used for data and theory (adapted from Ref. 9).

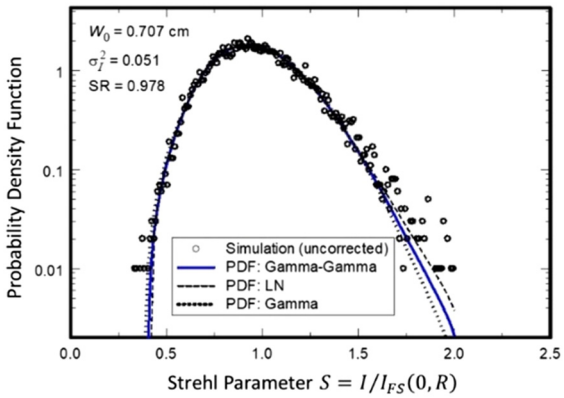

Fig. 26 Graph of three uplink beam PDFs as a function of Strehl parameter for $2W_0/r_{0\,tx} \ll 1$ with computer simulation results (Ref. 11, chapter 6).

Let us now look at how these equations agree with PDF computer simulations. The simulations to be discussed assumes an optical beam from ground to space in 1xHV5/7 turbulence with zero zenith angle and $\lambda = 1.55$ μm. The figures to come contain both computer simulation data and theoretical PDF models as a function of the Strehl parameter $S = I/I_{\mathrm{FS}}(0,R)$ featuring several beam sizes covering various regimes of interest (Ref. 11 in chapter 6). In the Strehl parameter, $I_{\mathrm{FS}}(0,R)$ is the mean free space transmitted intensity. The scintillation index and mean Strehl ratio in the legends of these figures are based on theoretical expressions, not simulation results. In all cases, the Fried parameter is 19 cm. As with the last two figures, the next few figures show good agreement between the theoretical and simulation data.

Figure 26 compares three uncorrected uplink beam PDFs as a function of Strehl parameter with computer simulation results (chapter 6 in Ref. 11). In this figure, we have $(2W_0/r_{0tx} = 0.074 \ll 1)$. In this case, the tracked and untracked scintillation indices are the same as there is no beam wander. The three PDFs in the following figures are the log-normal (LN), gamma–gamma (GG), and gamma (G) PDFs. The three PDFs appear to agree with one another until the Strehl parameter becomes greater than 1.5. The LN PDF appears to be closer to the data than the other two PDFs, but there are some outliers in the simulation results.

Figures 27 and 28 are comparisons of the untracked and tilt-corrected uplink beam PDFs as a function of the Strehl parameter with computer simulation results for $(0.1 < 2W_0/r_{0\mathrm{T}} < 10)$ using two different $W_0's$ (chapter 6 in Ref. 11). The PDF used in the (a) figures is an MG PDF and the one used in the (b) figures is a G PDF. It is clear from Figs. 27(a) and 28(a) that the increase in the size of W_0 causes the PDF shape to radically change. Figures 27(b) and 28(b) have similar shapes but not values.

Figure 29 shows a comparison of the untracked and tilt-corrected uplink beam PDFs as a function of Strehl parameter with computer simulation results for $(2W_0/r_{0\mathrm{T}} = 7.4)$ (chapter 6 in

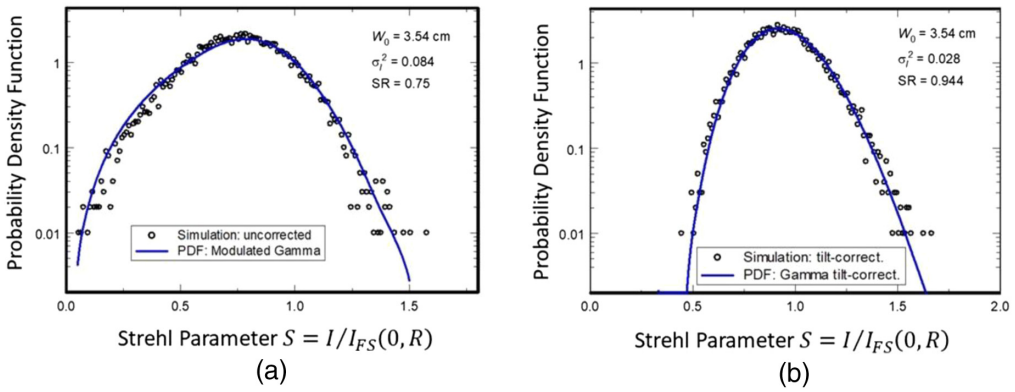

Fig. 27 Comparison of (a) untracked and (b) tilt-corrected uplink beam PDFs as a function of Strehl parameter for $(0.1 < 2W_0/r_{0\mathrm{T}} < 10)$ with computer simulation results (Ref. 11, chapter 6).

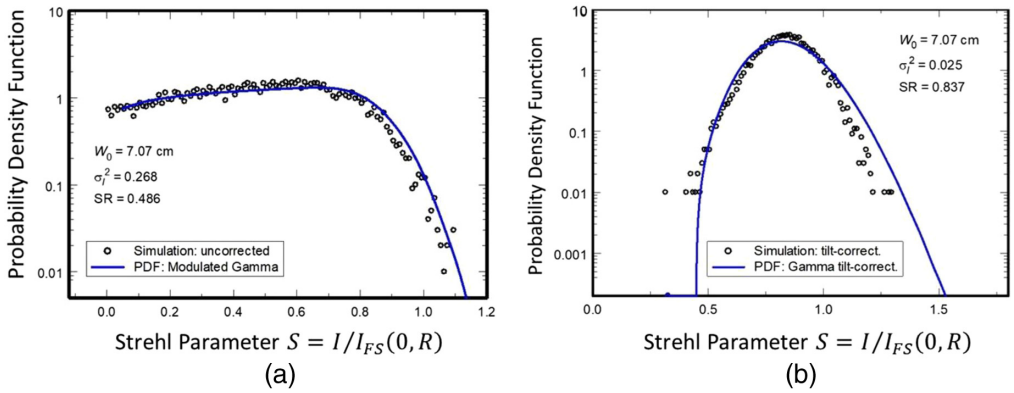

Fig. 28 Comparison of (a) untracked and (b) tilt-corrected uplink beam PDFs as a function of Strehl parameter for $(0.1 < 2W_0/r_{0T} < 10)$ with computer simulation results (Ref. 11, chapter 6].

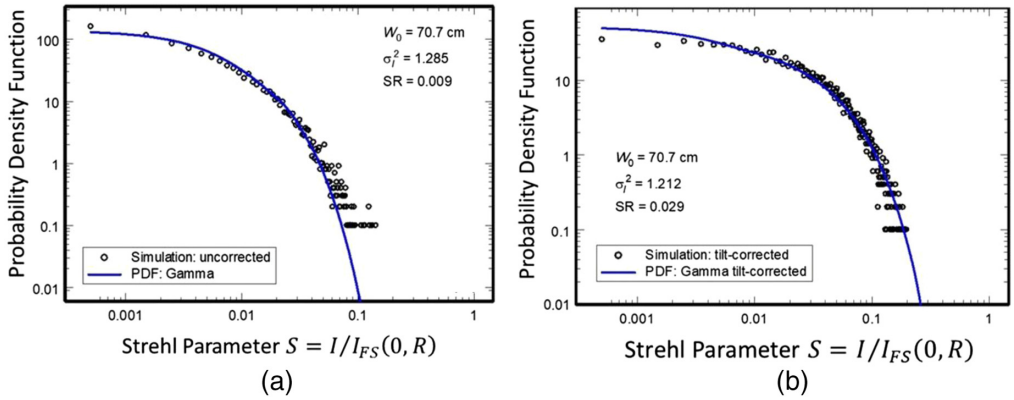

Fig. 29 Comparison of (a) untracked and (b) tilt-corrected uplink beam PDFs as a function of Strehl parameter for $(2W_0/r_{0T} = 7.4)$ with computer simulation results (chapter 6 in Ref. 11).

Ref. 11). The PDF used in the (a) figures is an MG PDF and the one used in the (b) figure is a G PDF. The untracked and tilt-corrected PDFs have more similar shapes but different values. The similarity comes from the fact that the large beam effectively means there is essentially no beam wander.

6.2 Downlink Communications Scintillation Indices

In this case, the beam will be essentially a collimated beam from the satellite. The scintillation index follows that of a plane wave propagating through turbulence contained in the near-earth atmosphere (angle of arrival fluctuations may be several microradians).[31] In fact, from space-to-ground the scintillation index (also equal to the Rytov variance in this case) is basically the same as that of an infinite plane wave and is given as

$$\sigma_I^2 \equiv \sigma_R^2 = 2.25k^{7/6}\, sec^{11/6}(\zeta) \int_{h_0}^{H} C_n^2(h)(h-h_0)^{5/6}\mathrm{d}h.\ H \gg 20\ \mathrm{km}. \tag{124}$$

If the receiver aperture is larger, then aperture averaging reduce scintillation. The aperture-averaged scintillation index is written as

$$\sigma_I^2(D_{rx}) = 8.70k^{7/6}(H-h_0)^{5/6}\,\mathrm{Re}\left\{\int_{h_0}^{H} C_n^2(h)\left[\left(\frac{kD_{rx}^2}{16R} + i\frac{(h-h_0)}{(H-h_0)}\right)^{5/6} - \left(\frac{kD_{rx}^2}{16R}\right)^{5/6}\right]\mathrm{d}h\right\}, \tag{125}$$

for 0 deg-zenith angle (Ref. 10, p. 106). For other zenith angles, Eq. (125) was modified for a slant path assuming the round Earth model. Figure 30 depicts the aperture-averaged scintillation index as a function of the receiver diameter for $\zeta = 0$ deg, 20 deg, 40 deg, and 60 deg. As the

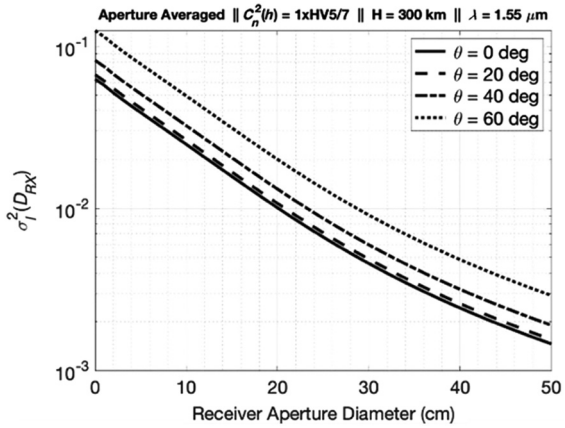

Fig. 30 Plot of the aperture averaged scintillation index $\sigma_I^2(D_{rx})$ as a function of the receiver diameter D_{rx} for four zenith angles.

receiver diameter gets larger, the aperture-averaged scintillation index gets smaller. For higher turbulence levels, the scintillation index for a point receiver is written as (Ref. 10, p. 106)

$$\sigma_I^2(L) = \exp\left[\frac{0.49\sigma_R^2}{(1+1.11\sigma_R^{12/5})^{7/6}} + \frac{0.51\sigma_R^2}{(1+0.69\sigma_R^{12/5})^{5/6}}\right] - 1. \tag{126}$$

Scintillation measurements of a 1064 nm laser were made by an optical ground station at the European Space Agency observatory in Tenerife, Spain, while tracking a low Earth orbit satellite during the spring and summer of 2010. Yura and Kozlowski reported the first comparison between theoretical predictions and these measurements.[43] Specifically, they compared Yura's apertured-averaged scintillation index (SI) model[44] evaluated using the MAUI3 turbulence profile model[45] against said data. Good agreement was obtained. The authors saw minor variation in the SI between daytime and nighttime experimental runs. In addition, their results suggested that the nighttime turbulence profile for the atmosphere above the observatory in Tenerife is like that above Haleakala in Maui, Hawaii.

Figure 31 compares the MAUI3 and AMOS refractive index structure parameter vertical profile models with a 0.1xHAP model where $C_n^2(h_0) = 5 \times 10^{-15}$ m$^{-2/3}$. The latter model follows the MAUI3 model well, except close to the ground. Comparing the MAUI3 profile with Figs. 19 and 20 for the Canary Islands and Hilo, respectively, the basic profile is similar among all three, but each is shifted relative to the others in $C_n^2(h)$ values. The modified HAP models do a good job in predicting each profile.

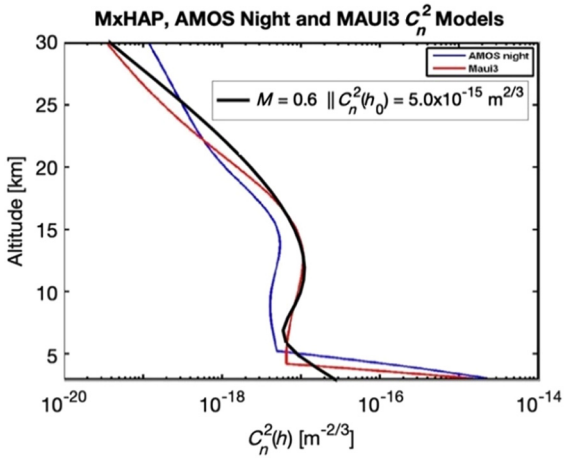

Fig. 31 Comparison of 0.6xHAP, MAUI3, and AMOS refractive index structure parameter vertical profile models.

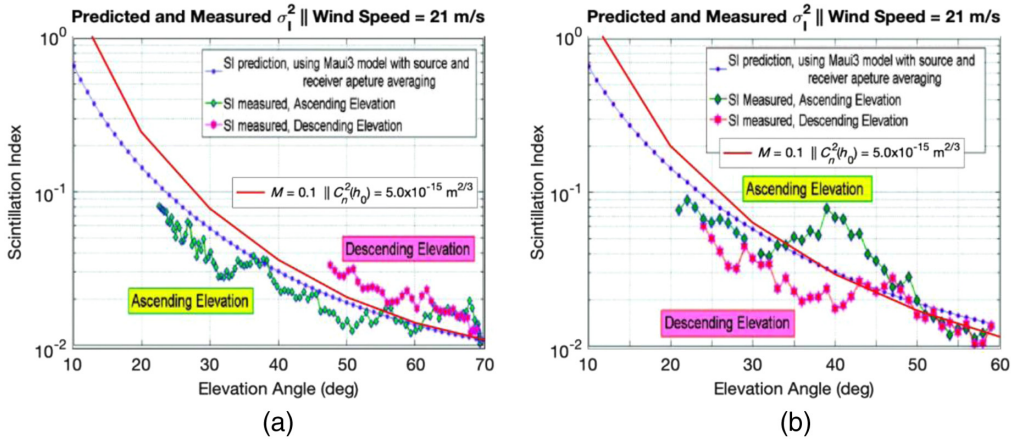

Fig. 32 Comparisons of measured SI data as a function of elevation angle for specific (a) daytime and (b) nighttime experiments with both the Yura SI model and Eq. (124) evaluated using the 0.1xHAP model.

Figure 32 compares SI measurements as a function of elevation angle for (a) daytime, 09:44:04 local time on June 23, 2010, and (b) nighttime, 24:27:00 local time on July 14, 2010, with both the Yura SI model[43] and Eq. (124) were evaluated using the 0.1xHAP model. The Eq. (124) predictions using the 0.1xHAP model follows the measurements as well as the Yura models do using the MAUI3 model. Like in the case of fiber coupling, we lower the multiplier in the $C_n^2(h)$ HAP model to get good agreement with measurements. Again, more definitive comparisons could be made if radiosonde or ground scintillometer measurements were made during the experimental runs.

Perlot et al.[46] reported a set of experimental measurements derived from the Japanese Optical Inter-orbit Communications Engineering Test Satellite (OICETS) communicating down to an optical receiver located near Munich, Germany. OICETS is an LEO satellite with a sun-synchronous orbit at an altitude of 610 km. It is optically compatible with the Artemis satellite and transmits a 50-Mbit/s NRZ OOK data stream at a wavelength of 847 nm. The experiment's ground receiver used a 40-cm (12-cm obscuration) Cassegrain telescope receiver. Figure 33 shows OICETS uplink scintillation index measurements derived from the received uplink as well as Eq. (121) predictions assuming a 0.4xHAP model with constant slew rate of 0.003 rad/s and $C_n^2(h_0) = 5 \times 10^{-15}$ m$^{-2/3}$. This figure shows reasonable agreement between analytical predictions and the measurements.

Figure 34 shows (a) various measured OICETS downlink scintillation indices created from the received downlink and (b) DIMM-based measurements of the Fried parameter r_0. Included in

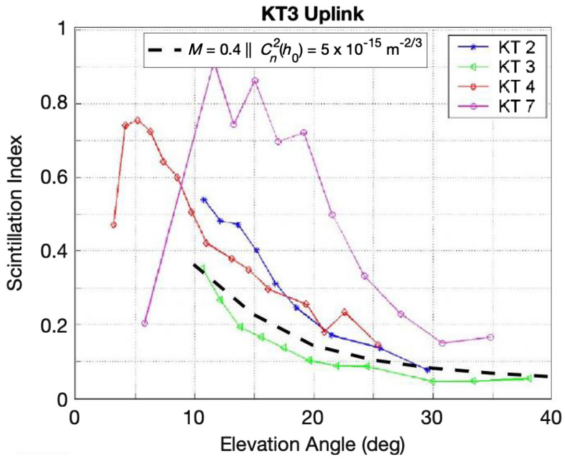

Fig. 33 Comparison of measured OICETS uplink scintillation indices and Eq. (121) assuming a 0.4xHAP Models with $C_n^2(h_0) = 5 \times 10^{-15}$ m$^{-2/3}$ and a constant slew rate of 0.003 rad/s.

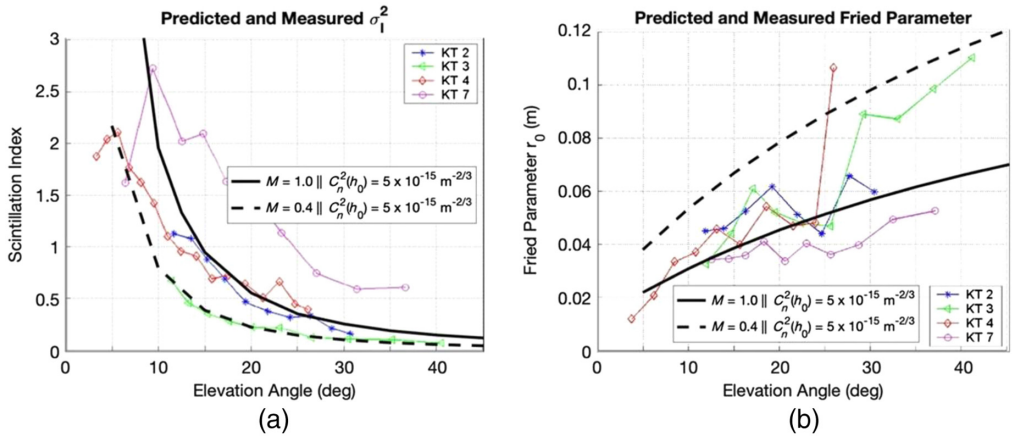

Fig. 34 Comparison of Eq. (125) and Fried parameter calculations for a 1xHAP and a 0.2xHAP models with (a) various measured OICETS downlink scintillation indices and (b) DIMM-based measurements for the Fried parameter r_0. The two models assumed $C_n^2(h_0) = 5 \times 10^{-15}$ m$^{-2/3}$ and a constant slew rate of 0.003 rad/s.

these figures are Eq. (125) and Fried parameter predictions using the 1xHAP and 0.4xHAP models assuming a constant slew rate of 0.003 rad/s and $C_n^2(h_0) = 5 \times 10^{-15}$ m$^{-2/3}$. The resulting wind speed was ~74 m/s. These figures show good agreement between analytical predictions and the various data sets. However, the OICETS satellite experiences a variable slew rate that is a function of the incurred elevation angle. Figure 35 is a redo of Fig. 34, but where only the 0.4xHAP model plus the Elevation Angle-Max = 90 deg slew rate curve given in fig. 10 of Ref. 46 are used to calculate Eq. (124) and Fried parameter predictions. Figure 34(a) also includes the Rytov variance, which is the non-aperture averaged scintillation index. In Fig. 34(a), the 0.4xHAP model scintillation index expands and deviates a little from the KT3 curve for elevation angles greater than 20 deg. Clearly, the aperture averaging drives the Rytov variance down a lot to yield the Eq. (125) curve. In Fig. 34(b), the resulting curve now reaches a peak at an elevation angle round 18 deg and then decreases. Its shape in more in line with all data curves, except the KT3 curve. It also shows that the variable slew rate has a dramatic effect on key turbulence parameters.

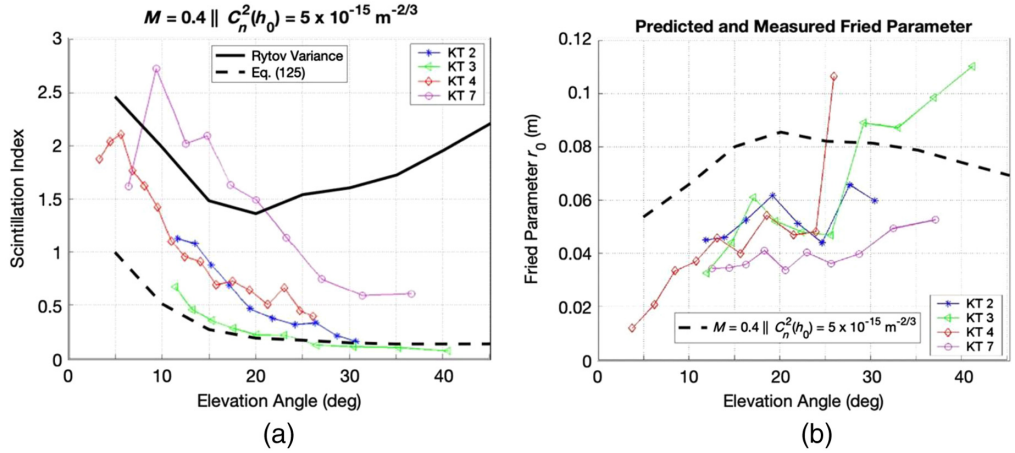

Fig. 35 Comparison of Eq. (125) and Fried parameter calculations for a 0.4xHAP models with (a) various measured OICETS downlink scintillation indices and (b) DIMM-based measurements for the Fried parameter r_0. The two models assumed $C_n^2(h_0) = 5 \times 10^{-15}$ m$^{-2/3}$ and the Elevation Angle-Max = 90 deg slew rate curve given in fig. 10 of Ref. 46.

6.3 Horizontal Communications Scintillation Index

This section deals with the scintillation index for a horizontal communications link, which involves Gaussian beam propagation. Because of the horizontal geometry, this path can exhibit strong beam wander and large scintillation indices. The following equations are from Ref. 9, section 10.3.5; Ref. 10, pp. 52–53.

For a horizontal FSOC link, the spherical-wave Fried parameters equal

$$r_{0tx} = r_{0rx} = [0.16k^2 C_n^2(h_{tx})R]^{-3/5}, \tag{127}$$

with $h_{tx} = h_{rx}$.

The beam wander variance and pointing error variance in the pupil plane are

$$\langle r_c^2 \rangle = 2.42 C_n^2(h_{tx}) R^3 W_0^{-1/3}, \tag{128}$$

and

$$\sigma_{pe}^2 = \frac{2.42 C_n^2(h_{tx}) R^3}{W_0^{1/3}} \left[1 - \left(\frac{\pi^2 W_0^2 / 25 r_0^2}{1 + \pi^2 W_0^2 / 25 r_0^2} \right)^{1/6} \right], \tag{129}$$

respectively. The beam wander variance and pointing error variance in the detector plane are

$$\langle r_c^2(D_{Rx}) \rangle = \frac{2.42 C_n^2 R^3}{W_0^{1/3}} \left(\frac{\Omega_{Rx}}{\Lambda_1 + \Omega_{Rx}} \right), \tag{130}$$

and

$$\sigma_{pe}^2(D_{Rx}) = \frac{2.42 C_n^2(h_{tx}) R^3}{W_0^{1/3}} \left(\frac{\Omega_{Rx}}{\Lambda + \Omega_{Rx}} \right) \left[1 - \left(\frac{\pi^2 W_0^2 / 25 r_0^2}{1 + \pi^2 W_0^2 / 25 r_0^2} \right)^{1/6} \right], \tag{131}$$

with $\Omega_{Rx} = 2R/k_0 W_{Rx}^2$ and $W_{Rx} = D_{rx}/2\sqrt{2}$.

The Rytov variance, long-term beam radius and short-term beam radius in the pupil plane are given as

$$\sigma_R^2 = 1.23 C_n^2(h_{tx}) k_0^{7/6} R^{11/6}, \tag{132}$$

$$W_{\mathrm{LT}} = W(1 + 1.33\sigma_R^2 \Lambda^{5/6})^{3/5}, \tag{133}$$

and

$$W_{\mathrm{ST}} = \sqrt{W_{\mathrm{LT}}^2 - \langle r_c^2 \rangle}. \tag{134}$$

The wander-induced scintillation index in the detector plane is equal to

$$\sigma_{I,\mathrm{Untracked}}^2(D_{Rx}) = 4.42 \frac{\sigma_R^2 \Lambda_{\mathrm{ST}}^{5/6} \sigma_{pe}^2}{W_{\mathrm{ST}}^2} + \exp[\sigma_{\ln X}^2(D_{Rx}, l_0) - \sigma_{\ln X}^2(D_{Rx}, l_0, L_0) + \sigma_{\ln Y}^2(D_{Rx})] - 1, \tag{135}$$

and the tip/tilt-tracked scintillation index in the detector plane equals

$$\sigma_{I,\text{Tip-Tilt}}^2 = \exp[\sigma_{\ln X}^2(D_{Rx}, l_0) - \sigma_{\ln X}^2(D_{Rx}, l_0, L_0) + \sigma_{\ln Y}^2(D_{Rx})] - 1, \tag{136}$$

with $\Lambda_{\mathrm{ST}} = 2R/k_0 W_{\mathrm{ST}}^2$. In Eqs. (135) and (136), we have

$$\frac{\sigma_{\ln X}^2(D_{Rx}, l_0)}{0.49\sigma_R^2} = \left(\frac{\Omega_{Rx} - \Lambda}{\Omega_{Rx} + \Lambda} \right)^2 \left(\frac{1}{3} - \frac{1}{2}\overline{\Theta} + \frac{1}{5}\overline{\Theta}^2 \right) \left(\frac{\eta_{Xd} Q_l}{\eta_{Xd} + Q_l} \right)^{7/6} \times \left[1 + 1.75 \left(\frac{\eta_{Xd}}{\eta_{Xd} + Q_l} \right)^{1/2} - 0.25 \left(\frac{\eta_{Xd}}{\eta_{Xd} + Q_l} \right)^{7/12} \right], \tag{137}$$

$$\frac{\sigma^2_{\ln X}\left(D_{Rx}, l_0, L_0\right)}{0.49\sigma_R^2} = \left(\frac{\Omega_{Rx}-\Lambda}{\Omega_{Rx}+\Lambda}\right)^2\left(\frac{1}{3}-\frac{1}{2}\bar{\Theta}+\frac{1}{5}\bar{\Theta}^2\right)\left(\frac{\eta_{Xd0}Q_l}{\eta_{Xd0}+Q_l}\right)^{7/6} \times\left[1+1.75\left(\frac{\eta_{Xd0}}{\eta_{Xd0}+Q_l}\right)^{1/2}-0.25\left(\frac{\eta_{Xd0}}{\eta_{Xd0}+Q_l}\right)^{7/12}\right], \tag{138}$$

$$\sigma^2_{\ln Y}(D_{Rx}, l_0) = \frac{1.27\sigma_R^2\eta_Y^{-5/6}}{1+0.40\eta_Y/(\Omega_{Rx}+\Lambda_1)}, \tag{139}$$

$$\eta_X = \left[0.38/(1-3.21\overline{\Theta}+5.92\bar{\Theta}^2)+0.47\sigma_R^2 Q_l^{1/6}\left(\left(\frac{1}{3}-\frac{1}{2}\overline{\Theta}+\frac{1}{5}\overline{\Theta}^2\right)/(1+2.20\overline{\Theta})\right)^{6/7}\right]^{-1}, \tag{140}$$

$$\begin{aligned}\sigma_G^2 \equiv \sigma_{I,l}^2(0,L) \approx 3.86\sigma_R^2\Bigg\{&0.40\frac{[(1+2\Theta)^2+(2\Lambda+3/Q_l)^2]^{11/12}}{[(1+2\Theta)^2+4\Lambda^2]^{1/2}} \\ &\times\left[\sin\left(\frac{11}{6}\varphi_2+\varphi_1\right)+\frac{2.610}{[(1+2\Theta)^2Q_l^2+(3+2\Lambda Q_l)^2]^{1/4}}\sin\left(\frac{4}{3}\varphi_2+\varphi_1\right)\right. \\ &\left.-\frac{0.518}{[(1+2\Theta)^2Q_l^2+(3+2\Lambda Q_l)^2]^{7/24}}\sin\left(\frac{5}{4}\varphi_2+\varphi_1\right)\right]-\frac{13.401\Lambda}{Q_l^{11/6}[(1+2\Theta)^2+4\Lambda^2]} \\ &-\frac{11}{6}\left[\left(\frac{1+0.31\Lambda Q_l}{Q_l}\right)^{5/6}+\frac{1.096(1+0.27\Lambda Q_l)^{1/3}}{Q_l^{5/6}}-\frac{0.186(1+0.24\Lambda Q_l)^{1/4}}{Q_l^{5/6}}\right]\Bigg\},\end{aligned} \tag{141}$$

and

$$\eta_Y = 3(\sigma_R/\sigma_G)^{12/5}(1+0.69\sigma_G^{12/5}), \tag{142}$$

where $\eta_{Xd0} = \eta_{Xd}\hat{Q}_0/(\eta_{Xd}+\hat{Q}_0)$, $\eta_{Xd} = \eta_X/[1+0.40\eta_X(2-\overline{\Theta}_1)/(\Omega_{Rx}+\Lambda_1)]$, $\hat{Q}_0 = 64\pi^2R/k_0L_0^2$, $Q_l = 10.89R/k_0l_0^2$, $\varphi_1 = \tan^{-1}(2\Lambda/[1+2\Theta])$, and $\varphi_2 = \tan^{-1}[(1+2\Theta)Q_l/(3+2\Lambda Q_l)]$.

Strömqvist Vetelino et al.[47] used Eq. (135) to compare resulting GG and LN PDF against both simulation and experimental data. The range is 1500 m. Figures 36–38 show example comparisons of GG and LN PDFs as a function of the normalized log irradiance $\ln(I)$ against simulation and experimental results for $D_{rx} = \sim$1,5, and 13 mm.[47] The authors cited $C_n^2(h_{tx}) = 6.45\times10^{-14}$ m$^{-2/3}$ for both the computer simulation and experiment. These figures show that both sets of data agreed with both PDFs in the middle but deviate from the LN PDF at

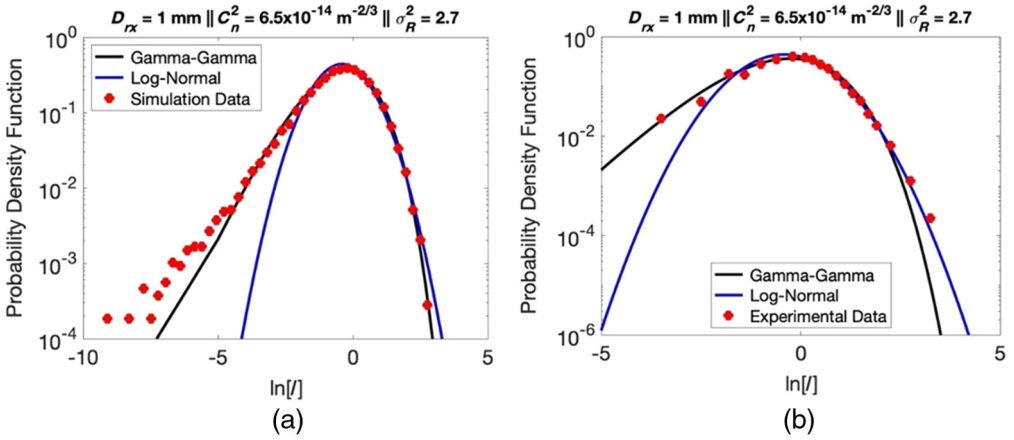

Fig. 36 Comparison of GG and LN PDFs as a function of the normalized log irradiance $\ln(I)$ against (a) simulation data and (b) experimental data for $D_{rx} = \sim$1 mm and $C_n^2(h_{tx}) = 6.5\times10^{-14}$ m$^{-2/3}$.

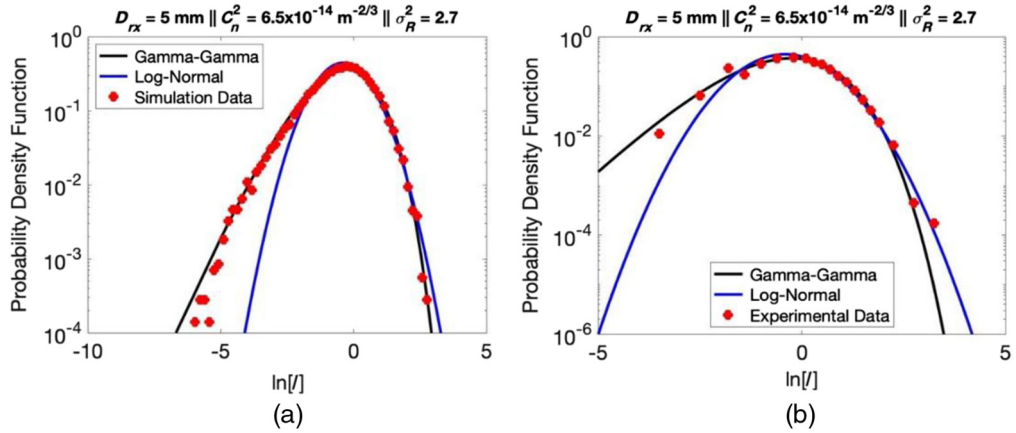

Fig. 37 Comparison of GG and LN PDFs as a function of the normalized log irradiance $\ln(I)$ against (a) simulation data and (b) experimental data for $D_{rx} = 5$ mm and $C_n^2(h_{tx}) = 6.5 \times 10^{-14}$ m$^{-2/3}$.

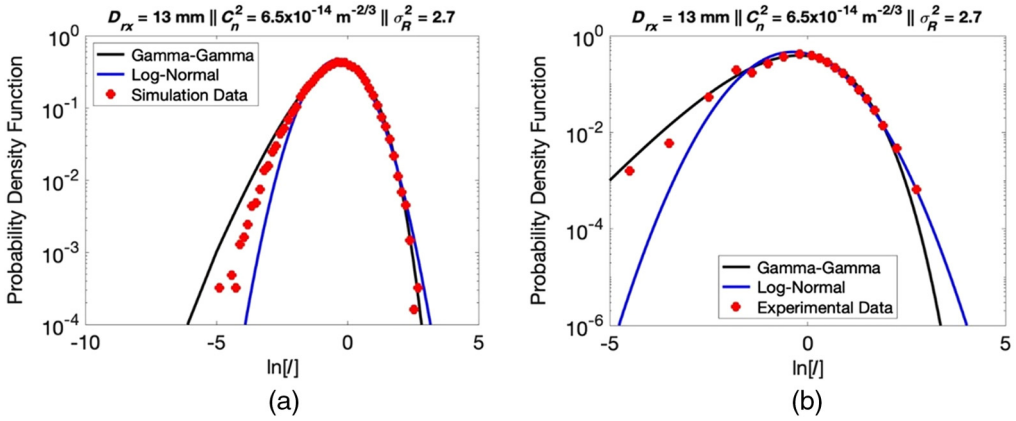

Fig. 38 Comparison of GG and LN PDFs as a function of the normalized log irradiance $\ln(I)$ against (a) simulation data and (b) experimental data for $D_{rx} = 13$ mm and $C_n^2(h_{tx}) = 6.5 \times 10^{-14}$ m$^{-2/3}$.

the tails for small intensities. However, both sets of data appear to follow the GG PDF well in that regime.

Figures 39–41 show example comparisons of GG, LN, and G PDFs as a function of the normalized log irradiance $\ln(I)$ against simulation and experimental results for receiver diameters, but with $C_n^2(h_{tx}) = 5.36 \times 10^{-13}$ m$^{-2/3}$.[47] These figures show that both sets of data agreed with all three PDFs in the middle. In Fig. 39(a), these data are closer to the GG PDF for small intensities but are closer to the LN PDF for high intensities. In Fig. 39(b), no data are available for a comparison at small intensities, but other runs showed data closer to GG again. The exhibited data are still closer to the LN PDF for high intensities. The next five figures show that both the simulation and experimental data follow the LN PDF.

Their conclusion was that in the moderate-to-strong fluctuation regime, the GG distribution provides a good fit to the irradiance fluctuations collected by finite-sized apertures that are significantly smaller than the lateral spatial coherence radius ρ_0. For apertures larger than or equal to this radius, the irradiance fluctuations are LN distributed. We noted this trend when discussing intensity PDFs earlier in this paper.

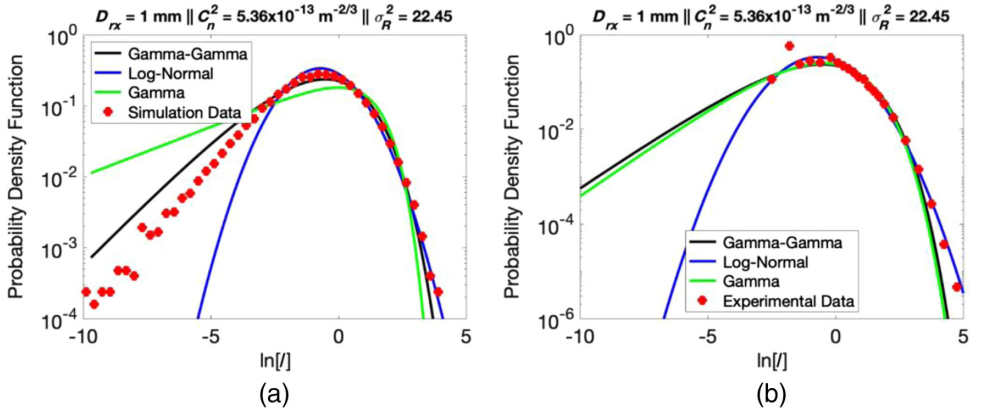

Fig. 39 Comparison of G, GG, and LN PDFs as a function of the normalized log irradiance $\ln(I)$ against (a) simulation data and (b) experimental data for $D_{rx} = \sim 1$ mm and $C_n^2(h_{tx}) = 5.36 \times 10^{-13}$ m$^{-2/3}$.

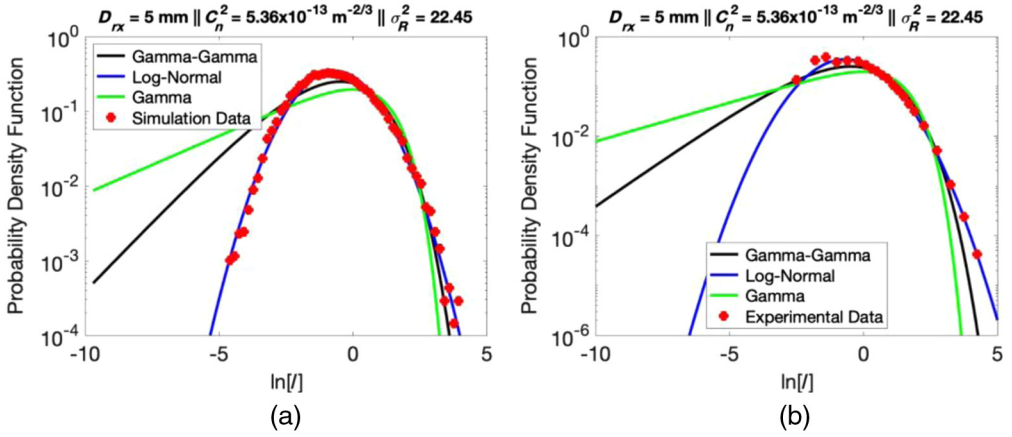

Fig. 40 Comparison of G, GG, and LN PDFs as a function of the normalized log irradiance $\ln(I)$ against (a) simulation data and (b) experimental data for $D_{rx} = 5$ mm and $C_n^2(h_{tx}) = 5.36 \times 10^{-13}$ m$^{-2/3}$.

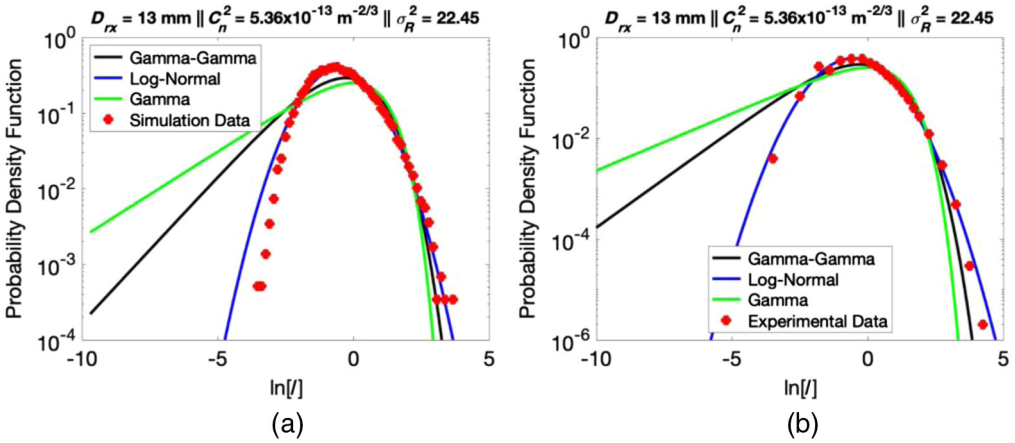

Fig. 41 Comparison of G, GG, and LN PDFs as a function of the normalized log irradiance $\ln(I)$ against (a) simulation data and (b) experimental data for $D_{rx} = 13$ mm and $C_n^2(h_{tx}) = 5.36 \times 10^{-13}$ m$^{-2/3}$.

Table 5 Comparison of Fried parameters and tracked, tip/tilt-corrected scintillation indices for HAP and 1xHV/5/7 models yielding the same Fried parameter at $\zeta = 0$ deg.

Zenith angle	0 deg	20 deg	40 deg	60 deg
HAP model r_{ot} (cm)	19.4	18.7	16.5	12.8
1xHV/5/7 model r_{ot} (cm)	19.4	18.7	16.5	12.8
HAP model r_{or} (m)	9.56	9.14	8.18	6.43
1xHV/5/7 model r_{or} (m)	17.57	17.44	16.80	14.69
HAP model tracked $\sigma_l^2(0, R)$	0.105	0.115	0.152	0.265
1xHV/5/7 model tracked $\sigma_l^2(0, R)$	0.027	0.029	0.039	0.067

7 Example BER Calculation and Turbulence Mitigation

In this section, we provide an example of BER calculations. If they do not meet the system BER requirement, we will provide a couple of techniques that will show these BERs can be improved. These latter techniques are for illustrative purposes only and not intended to imply these are the only options or the best. However, they both do work in turbulent situations where amplitude fluctuations dominate unlike adaptive optics.[12]

In reviewing the literature, one finds a few ways of specifying the atmospheric turbulence levels for SATCOM link budget calculations. One way is to specify the Fried parameter for the envisioned scenario. For example, let us assume a 19 cm Fried parameter for a 0-deg zenith angle SATCOM link. Table 5 exhibits a comparison of Fried parameters and tracked/tilt-corrected and untracked scintillation indices for the HAP and HV5/7 models yielding that assumed Fried parameter. We have assumed the following parameters for the HAP model are

$$h_G = 5 \text{ m}, \; h_0 = 1 \text{ m}, \; M = 4, \; C_n^2 = 5 \times 10^{-14} \text{ m}^{-2/3}.$$

These parameters are chosen so that the Fried parameter would match that of the 1xHV-5/7 model. It is clear from this table that the HAP models predict much larger scintillation indices than the 1xHV5/7 model even though the Fried parameters are the same. (It should be noted that the receiver Fried parameters yield unity Strehl ratios for all zenith angles.) Let us now look at example link budgets and BER plots for the 1xHV5/7 numbers in Table 5.

Let us assume that we have tip/tilt-corrected, 10 Gigabit per second (Gbps) EDFA-PIN uplink SATCOM link with the following system parameters: $P_r = 0$ dBm $= GP_{\text{avg}}$ for "1" signal, BER $= 10^{-12}$, $H = 300$ km, $F = \infty$, $D_{tx} = D_{rx} = 0.10$ m, $\eta = 0.681$, $\gamma_{tx} = \gamma_{rx} = 0.25$, $\lambda = 1.55$ μm, $B_e = 7.5$ GHz, and $n_{\text{sp}} = 1.58$ $[N_{\text{opt}} = 5 \text{ dB}]$. The atmospheric transmittance is derived from a Rural (VIS = 23 km) aerosol model atmosphere from 2-m above ground level

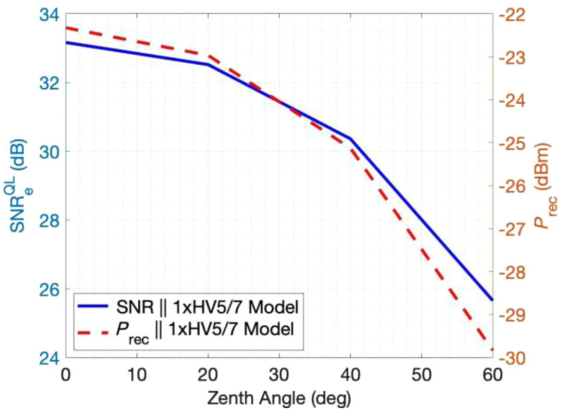

Fig. 42 Quantum-limited electrical SNR and received power as a function of SATCOM zenith angle for a 1xHV5/7 SATCOM uplink.

to space and is calculated using PCModWin®.[28] These transmittances were around 90% or higher and have negligible effect on the SNR for this analysis.

Figure 42 shows the average quantum-limited electrical SNR and received power as a function of SATCOM zenith angle. These SNRs are in the range for a reasonable gain to yield 0 dBm. (Note: One must be careful in applying gain to the input signal, so the result does not destroy the photodetector.)

From Table 4, the NRZ OOK BER in the absence of turbulence is given as

$$\overline{\mathrm{BER}} = 0.5 erfc\left(\sqrt{\mathrm{SNR_e}}/2^{3/2}\right). \tag{143}$$

For a tracked uplink, the average BER for NRZ-OOK then is

$$\overline{\mathrm{BER}} = 0.5\int_0^\infty p_I(I')erfc\left(\frac{1}{2^{3/2}}\sqrt{\frac{\mathrm{SNR_e^{QL}}(I')^2}{\eta NF_{\mathrm{opt}}I' + \mathrm{SNR_e^{QL}}\sigma_{I,l}^2(0,R)_{\mathrm{Tracked}}}}\right)\mathrm{d}I', \tag{144}$$

using Eq. (101) but with Eq. (110) replacing the LN PDF. Figure 43 shows BER performance as a function of the $\mathrm{SNR_e^{QL}}$ for selected zenith angles. The required 10^{-12} BER is not achieved even though $\mathrm{SNR_e^{QL}}$ is large at any of the zenith angles shown. In fact, the BER essentially limits out for $\mathrm{SNR_e^{QL}} > 25$ dB at all zenith angles at values orders of magnitude larger. As it turns out, whether the system is incoherent or coherent and/or which signaling format is used, the scintillation index will peg the BER to constant value at high SNR well above the BER requirement. Other turbulence mitigation techniques must be employed to get the desired system performance, e.g., interweaving forward error correction (FEC) coding, optical automatic gain control (OAGC) circuitry.

Using a Reed-Solomon FEC Code RS(255,199), the BER performance can be improved to levels better than the BER requirement as shown in Fig. 44, e.g., at $\zeta = 60$ deg, the BER is $<10^{-14}$. The penalty is that the information rate drops by the ratio of $199/255 = 0.78$. This is a small price to pay given the significant BER performance improvements. [A RS(255,207) code allows all the zenith angle but $\zeta = 60$ deg to exceed the 10^{-12} BER requirement. At $\zeta = 60$ deg, the BER is level at $\sim 8 \times 10^{-12}$.]

An alternative for OOK and DPSK systems is to use the optical automatic gain control invented by David Young from John Hopkins University Applied Physics Laboratory.[8,48] It basically reduces the variance in the intensity PDF under long range/high turbulence conditions, among other things.[8,49] Let us be more specific.

Figure 45 shows the high-level layout of the OAGC. The first function of the OAGC system is protection of the photodiodes and follow-on electronics from catastrophic damage caused by high received optical powers at the output of the FSOC terminal.[8,48] To prevent this, the OAGC

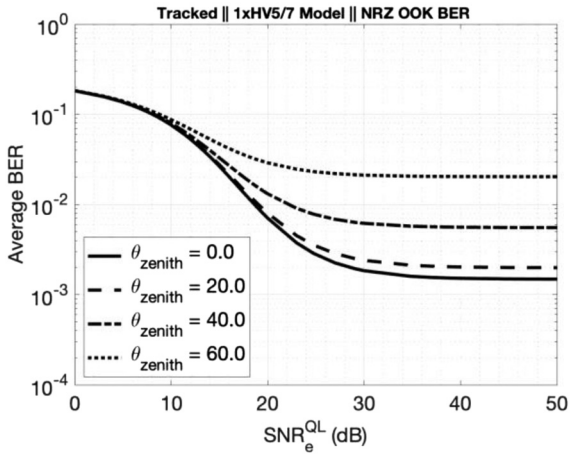

Fig. 43 1xHV5/7 BER performance as a function of quantum-limited electrical SNR for selected zenith angles.

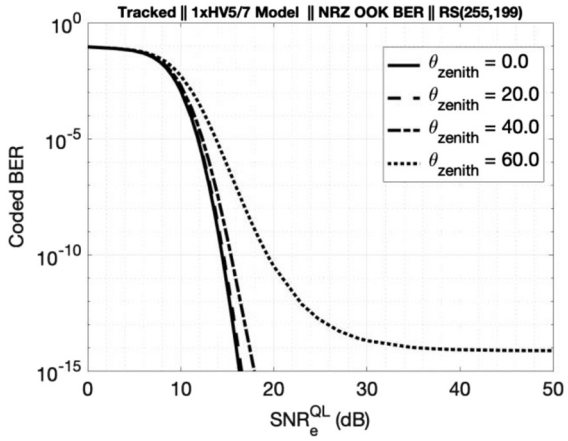

Fig. 44 1xHV5/7 BER using the RS(255,199) code as a function of quantum-limited electrical SNR for selected zenith angles.

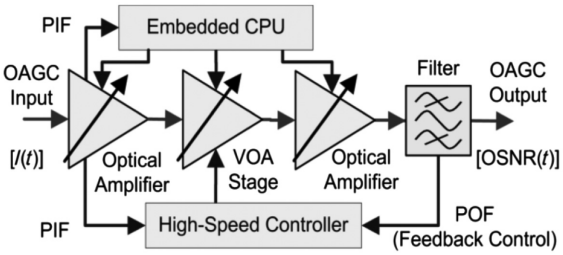

Fig. 45 OAGC block diagram (CPU = central processing unit).[49]

optically amplifies or attenuates as necessary through a series of multiple gain stages as presented in Fig. 45 and discussed in Ref. 49 to output a constant power at a level of optimal performance for the detector. In essence, the time-variant optical input $[I(t)]$ is translated into a constant amplitude output with a variable optical signal-to-noise ratio [OSNR(t)]. This is shown in Fig. 46, which presents OSNR and OAGC output power as a function of power into the OAGC (PIF). The maximum gain of the first-generation system was between 40 and 45 dB.[49]

The second function of the OAGC is to provide low-noise optical amplification for improved receiver sensitivity. This aspect of performance is characterized by the noise figure (NF) and gain metrics.[8] Because the system NF is set by the first amplifier, this stage is designed for low NF and only has a moderate net gain. In addition, it is designed to gain clamp at input levels above a certain level to aid in maintaining the desired system output. The second stage incorporates a

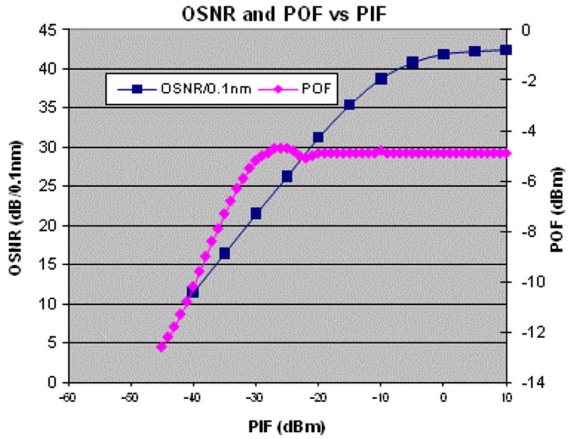

Fig. 46 OAGC block diagram (CPU = central processing unit).[8]

variable optical attenuator with a response time of <4 μs to dynamically respond to input power fluctuations by adjusting the system gain. The third stage handles output regulation and is designed to manage higher output power with an adjustable gain. For the overall system gain metric, the effective OAGC gain is dependent on the pre-set target output level. The third function of the OAGC is to reduce bit errors arising from power fluctuations at the receiver that cause timing jitter in the digital eye. By maintaining a constant output, power transients are prevented from coupling through the follow-on electronics and degrading BER performance in the FSOC link. This performance was shown in Fig. 22 for a 10^{-12} BER, which presents OSNR and OAGC output power as a function of power into the OAGC (which is equivalent to PIF) for 183 km link under 5xHV5/7 conditions.[8] The signal modulation scheme was NRZ-OOK. In short, the OAGC reduces the turbulent-intensity PDF to "delta function" (upper righthand corner) eliminating the PDF integration in Eq. (101) and leaving one with the mean intensity as a result.

8 Summary

This paper provided a tutorial on how to create link budgets and BER and probability of fade calculations for optical communications designed to operate in the turbulent channel. It reviewed the characterization models necessary for either incoherent or coherent FSOC uplink, downlink, and horizontal system analyses in the turbulent channel. Beam wander, scintillation, and receiver noise variance as well as pointing and tracking effects were included in this paper. Comparisons among these models, computer simulations, and field measurements are provided throughout the paper. Good agreement is shown among all. An example analysis was provided using this information. The conclusion is that no matter whether the system is incoherent or coherent and/or which signaling format is used, the scintillation index will peg the BER to constant value at high SNR well above the desired value. Other turbulence mitigation techniques must be employed to get the desired system performance.

Disclosures

The authors declare that there are no conflicts of interest related to this article.

Code and Data Availability

Experimental data presented in this paper may be obtained from the cited authors upon reasonable request.

References

1. C. Chen et al., "Demonstration of a bidirectional coherent air-to-ground optical link," *Proc. SPIE* **10524**, 105240G (2018).
2. H. Kaushal and G. Kaddoum, "Optical communication in space: challenges and mitigation techniques," *IEEE Commun. Surv. Tutorials* **19**(1), 57–96 (2017).
3. L. B. Stotts, *Free Space Optical Systems Engineering*, John Wiley and Sons (2017).
4. A. Mansour, R. Mesleh, and M. Abaza, "New challenges in wireless and free space optical communications," *Opt. Lasers Eng.* **89**, 95–108 (2017).
5. S. Seel et al., "Space to ground bidirectional optical communications link at 5.6 Gbps and EDRS connectivity outlook," in *Aerosp. Conf.*, Big Sky, Montana, pp. 1–7 (2011).
6. R. Lange et al., "142 km, 5.625 Gbps free: space optical link based on homodyne BPSK modulation," *Proc. SPIE* **6105**, 61050A (2006).
7. Z. C. Bagley et al., "Hybrid optical radio frequency airborne communications," *Opt. Eng.* **51**, 055006 (2012).
8. J. C. Juarez et al., "Analysis of link performance for the FOENEX laser communications system (Proceedings Paper)," *Proc. SPIE* **8380**, 838007 (2012).
9. L. C. Andrews and R. L. Phillips, *Laser Beam Propagation through Random Media*, 2nd ed., SPIE Press, Bellingham, Washington (2005).
10. L. C. Andrews. *Field Guide to Atmospheric Optics*, 2nd ed., SPIE Press, Bellingham, Washington (2019).
11. L. C. Andrews and M. K. Beason, *Laser Beam Propagation through Random Media: New and Advanced Topics*, SPIE Press, Bellingham, Washington (2023).
12. L. B. Stotts and L. C. Andrews, "An adaptive optics model characterizing turbulence mitigation for free space optical communications link budgets," *Opt. Express* **29**(13), 20307–20321 (2021).

13. S. O. Rice, "The mathematical analysis of random noise," *Bell Syst. Tech. J.* **23**, 282–332; 24, 46-256 (1945).
14. L. Mandel, "Fluctuations of photon beams; the distribution of photoelectrons," *Proc. Phys. Soc.* **74**, 233–243 (1959).
15. C. W. Helstrom, "The detection and resolution of optical signals," *IEEE Trans. Inf. Theory* **10**(4), 275–287 (1964).
16. A. Papoulis, *Systems and Transforms with Applications in Optics*, McGraw-Hill (1968).
17. V. I. Tartarski, *Wave Propagation in a Turbulent Medium*, McGraw-Hill (1961).
18. D. O. North, "An analysis of the factors which determine sign/noise discrimination in pulsed-carrier systems," RCA Tech Rept., PTR-6C, June 25, 1943 (ATI 24009). Reprinted in *Proc. IEEE* **51**, 1016–1027 (1963).
19. D. Middleton, "Statistical criteria for the detection of pulsed carriers in noise," *J. Appl. Phys.* **24**, 371–378 (1953).
20. W. W. Peterson, T. G. Birdsall, and W. C. Fox, "The theory of signal detectability," *Trans. IRE Prof. Group Inf. Theory* **4**, 171–212 (1954).
21. C.W. Helstrom, *Statistical Theory of Signal Detection*, 2nd ed., Pergamon Press (1968).
22. C. E. Shannon, "A mathematical theory of communication," *Bell Syst. Tech. J.* **27**, 379–423; 623–656 (1948).
23. H. Pishro-Nik, *Introduction to Probability, Statistics, and Random Processes*, Subsection 6.1.2, pp. 321–323, Kappa Research LLC (2014),
24. P. Becker, N. Olsson, and J. Simpson, *Erbium-Doped Fiber Amplifiers Fundamentals and Technology*, Academic Press (1999).
25. R. G. Marshalek, "Pointing, acquisition and tracking," Chapter 3 in *Near-Earth Laser Communications*, H. Hemmati, Ed., pp. 59–96, CRC Press (2009).
26. M. Toyoshima et al., "Optimum divergence angle of a Gaussian beam wave in the presence of random jitter in free-space laser communication systems," *J. Opt. Soc. Am. A* **19**(3), 567–571 (2002).
27. R. R. Beland, "Propagation through atmospheric optical turbulence," Chapter 2 in *The Infrared & Electro-Optical Systems Handbook*, W. L. Wolfe and G. J. Zissis, Eds., Vol. **2**, Environmental Research Institute of Michigan (1996).
28. L. B. Stotts and J. Schroeder, *Atmospheric Modeling Using PcModWin/MODTRAN*, SPIE Press, Bellingham, Washington (2019).
29. Y. Dikmelik and F. M. Davidson, "Fiber-coupling efficiency for free-space optical communication through atmospheric turbulence," *Appl. Opt.* **44**(23), 4946–4951 (2005).
30. L. C. Andrews, R. L. Phillips, and C. Y. Hopen, *Laser Beam Scintillation with Applications*, SPIE Press, Bellingham, Washington (2001).
31. L. B. Stotts and L. C. Andrews, "Bit error rate performance of a laser ground-to-satellite uplink communications systems in the presence of atmospheric turbulence and loss," in *Proc. 2022 IEEE Int. Conf. Space Opt. Syst. and Appl. (ICSOS)*, 28–31 March, Kyoto, p. a-16 (2022).
32. H. Takenaka, M. Toyoshima, and Y. Takayama, "Experimental verification of fiber-coupling efficiency for satellite-to-ground atmospheric laser downlinks," *Opt. Express* **20**(14), 15301–15308 (2012).
33. M. Toyoshima, H. Takenaka, and Y. Takayama, "Atmospheric turbulence-induced fading channel model for space-to-ground laser communications links," *Opt. Express* **19**(17), 15965–15975 (2011).
34. K. Yano, T. Yoshihisa, and K. Gyoda, "Measurements of the refractive index structure constant and studies on beam wander," in *Proc. Int. Conf. Space Opt. Syst. and Appl. ICSOS) 2014*, P-15 (2014).
35. International Telecommunication Union (ITU), "Propagation data required for the design of earth-space systems operating between 20 THz and 375 THz," ITU-RP.1621-2.
36. D. L. Walters and K. E. Kunkel, "Atmospheric modulation transfer function for desert and mountain locations: the atmospheric effects on r0," *J. Opt. Soc. Am.* **71**, 397–405 (1981).
37. L. B. Stotts and L. C. Andrews, "Improving the Hufnagel-Andrews-Phillips refractive index structure parameter model using turbulent intensity," *Opt. Express* **31**(9), 14265–14277 (2023).
38. H. A. Pike, private communications.
39. B. García-Lorenzo, J. J. Fuensalida, and M. A. C. Rodríguez-Hernández, "Statistical turbulence vertical profiles at the Roque de los Muchachos Observatory and Teide Observatory," *Proc. SPIE* **6747**, 67470C (2007).
40. F. Quatresooz, D. Vanhoenacker-Janvier, and C. Oestges, "Computation of optical refractive index structure parameter from its statistical definition using radiosonde data," *Radio Sci.* **58**(1), e2022RS007624 (2023).
41. D. A. Mahmood et al., "Improving Hufnagel-Andrews-Phillips model for prediction using empirical wind speed profiles," *J. Atmos. Solar-Terr. Phys.* **240**, 105952 (2022).
42. G. J. Baker and R. S. Benson, "Gaussian-beam weak scintillation on ground-to-space paths: compact descriptions and Rytov-method applicability," *Opt. Eng.* **44**, 106002 (2005).
43. H. T. Yura and D. A. Kozlowski, "Low Earth orbit satellite-to-ground optical scintillation: comparison of experimental observations and theoretical predictions," *Opt. Lett.* **36**(13), 2507–2509 (2011).
44. H. Yura and W. McKinley, "Aperture averaging of scintillation for space-to-ground optical communication applications," *Appl. Opt.* **22**, 1608–1609 (1983).

45. L. W. Bradford, "Maui4: a 24-hour Haleakala turbulence profile," in *Proc. Adv. Maui Opt. and Space Surveill. Technol. Conf. (AMOS 2010)*, pp. 499–516 (2010).
46. N. Perlot et al., "Results of the optical downlink experiment KIODO from OICETS satellite to Optical Ground Station Oberpfaffenhofen (OGS-OP)," *Proc. SPIE* **6457**, 645704 (2007).
47. F. Strömqvist Vetelino et al., "Aperture averaging effects on the probability density of irradiance fluctuations in moderate-to-strong turbulence," *Appl. Opt.* **46**(11), 2099–2106 (2007).
48. L. B. Stotts et al., "Hybrid optical RF airborne communications," *Proc. IEEE* **97**, 1109–1127 (2009).
49. J. C. Juarez et al., "High-sensitivity DPSK receiver for high-bandwidth free-space optical communication links," *Opt. Express* **19**(11), 10789–10796 (2011).

Larry B. Stotts is a consultant. His interest areas are RF and optical communications, and RF, infrared, and visible surveillance, and reconnaissance. He received his BA degree in applied physics and information sciences and his PhD in electrical engineering (communications systems), both from the University of California at San Diego. He has published over 113 journal articles and authored/co-authored four books. He is a fellow of the IEEE, SPIE, and Optica.

Larry C. Andrews is a Professor Emeritus of Mathematics at the University of Central Florida (UCF) and an associate member of the Townes Laser Institute in the College of Optics/CREOL at UCF. He received his PhD in theoretical mechanics from Michigan State University. He has authored/coauthored 12 textbooks and has published numerous papers and reports. He is a fellow of SPIE and authored three SPIE field guides.